Andean Geology 53 (2): 266-293. May, 2026
doi: 10.5027/andgeoV53n2-3878

Andean Geology
www.andeangeology.cl

SPECIAL ISSUE: RESEARCH ON THE SOUTH WEST MARGIN OF GONDWANA

An Early Pennsylvanian thermal anomaly in the forearc of SW Gondwana: the origin of the Caleta Loa Metamorphic Complex, northern Chile (21°30' S)

***Fernando Sepúlveda[1]; Paulina Vásquez[1]; Andrea Hemmelmann[2]; Gerhard Franz[2]**

[1] *Servicio Nacional de Geología y Minería, Chile. Avenida Santa María 0104, Providencia, Santiago. fernando.sepulveda@sernageomin.cl, paulina.vasquez@sernageomin.cl*

[2] *Institut für Angewandte Geowissenschaften, Technische Universität Berlin, 10587 Berlin, Germany. andrea_bhh@hotmail.com, gerhard.franz@tu-berlin.de*

* *Corresponding author: fernando.sepulveda@sernageomin.cl*

ABSTRACT. This study presents a comprehensive characterization of the Lower Pennsylvanian Caleta Loa Metamorphic Complex (CLMC), located in the Coastal Cordillera of northern Chile at around 21°30′ S. Through integrated petrographic, geochemical, thermodynamic, and geochronological analyses, the research aims to constrain the pressure-temperature (P-T) conditions of migmatite formation, refine the protolith identity, and assess the regional geodynamic context of the complex. Thermodynamic modelling using P-T pseudosections and mineral composition reveals that the CLMC migmatites formed under upper amphibolite facies conditions, with peak estimates of approximately 3.3-3.4 kbar and 650 °C. These results are consistent with a high geothermal gradient and suggest a crustal depth of ~13 km during peak metamorphism. U-Pb detrital zircon age patterns indicate a protolith sedimentation age no older than *ca.* 350 Ma (Early Mississippian), consistent with a genetic correlation with the nearby El Toco Formation, a low-grade metasedimentary unit in the forearc of the SW Gondwana margin. Structural data show evidence of compressional deformation, including top-to-the-west shear indicators and westward verging folds, which are interpreted as syn-anatectic features. These observations, combined with the metamorphic and geochronological data, point to a tectono-thermal event in the SW Gondwana forearc during the Early Pennsylvanian (*ca*. 318-316 Ma), associated with the so-called 'Toco Orogeny' and potentially linked to contemporaneous inland magmatic activity. The existence of this event supports a scenario of renewed subduction and/or the end of a magmatic lull along the proto-Pacific Gondwana margin. The current juxtaposition of the CLMC and the El Toco Formation on either side of a major fault suggests significant uplift and exhumation of the former prior to the Late Triassic.

Keywords: Migmatites, P-T pseudosections, 'Toco Orogeny', Carboniferous, SW Gondwana.

RESUMEN. Una anomalía termal del Pennsylvaniano Temprano en el antearco de Gondwana suroccidental: el origen del Complejo Metamórfico Caleta Loa, norte de Chile (21°30' S). Este estudio presenta una caracterización exhaustiva del Complejo Metamórfico Caleta Loa (CMCL), del Pennsylvaniano Inferior, situado en la Cordillera de la Costa del norte de Chile (~21°30′ S). Mediante análisis integrados de petrografía, geoquímica, termodinámica y geocronología, la investigación tiene como objetivo determinar las condiciones de presión-temperatura (P-T) de la formación de sus migmatitas, refinar la identidad del protolito y evaluar el contexto geodinámico regional del complejo. La modelización termodinámica, utilizando pseudosecciones P-T y composición mineral, revela que las migmatitas del CMCL se formaron en condiciones de facies anfibolita superior, con estimaciones máximas de aproximadamente 3,3-3,4 kbar y 650 °C. Estos resultados son consistentes con un gradiente geotérmico elevado y sugieren una profundidad cortical de aprox. 13 km durante el peak metamórfico. Los patrones de edad U-Pb de circones detríticos indican una edad máxima de sedimentación del protolito de *ca*. 350 Ma (Mississippiano Temprano), lo que concuerda con una correlación genética con la contigua Formación El Toco, unidad metasedimentaria de bajo grado metamórfico en el antearco del margen suroccidental de Gondwana. Los datos estructurales muestran evidencia de deformación compresiva, incluyendo indicadores de cizalle de bloque superior hacia el oeste y pliegues con vergencia hacia el oeste, que se interpretan como características sinanatécticas. Estas observaciones, combinadas con datos metamórficos y geocronológicos, apuntan a un evento tectono-termal en el antearco de Gondwana suroccidental durante el Pennsylvaniano temprano (*ca*. 318-316 Ma), asociado a la denominada

"Orogenia Toco" y potencialmente vinculado a actividad magmática continental contemporánea. La existencia de este evento respalda un escenario de subducción renovada y/o el fin de una fase de calma magmática a lo largo del margen proto-Pacífico de Gondwana. La yuxtaposición actual del CMCL y de la Formación El Toco a ambos lados de una falla importante sugiere alzamiento y exhumación significativos del CMCL antes del Triásico Tardío.

Palabras clave: Migmatitas, Pseudosecciones P-T, "Orogenia Toco", Carbonífero, Gondwana suroccidental.

1. Introduction

The western margin of South America once formed the SW margin of Gondwana (Fig. 1A). This area has been regarded as an active margin for almost the entire Palaeozoic Era, associated with the collision of tectono-stratigraphic terranes that were amalgamated to the supercontinent (*e.g*., Dalziel and Forsythe, 1985; Mpodozis and Ramos, 1989; Bahlburg and Hervé, 1997; Ramos, 2009). These successive events were part of the intercontinental accretionary Terra Australis Orogeny (Cawood, 2005), associated with changes in the conditions of subduction of the proto-Pacific oceanic plate under the continental margin of Gondwana (Vaughan *et al.*, 2005). Although some of these events are well studied and constrained in time, others are yet to be completely understood. The 'Toco Orogeny' (Bahlburg and Breitkreuz, 1991), for instance, is one of the latter, recorded in Upper Devonian-Lower Carboniferous low-grade marine metasedimentary successions of the Coastal Cordillera of northern Chile.

In northern Chile (18-32° S), several Palaeozoic metamorphic complexes are found as part of the SW Gondwana margin, in both the Coastal Cordillera and the Main Cordillera (*e.g.*, Hervé *et al.*, 2007; Pankhurst *et al.*, 2016; Díaz-Alvarado *et al*., 2019; Creixell *et al.*, 2021) (Fig. 1B). The Caleta Loa Metamorphic Complex (CLMC, Vásquez *et al.*, 2018; Fig. 1C), in the Coastal Cordillera, is a migmatite complex that provides evidence of a Late Carboniferous high-temperature magmatic/tectonic event. It is the northernmost example of melt generation associated with subduction at the SW Gondwana margin after the Devonian Period (see Creixell *et al.,* 2021).

The Devonian Period has traditionally been regarded as a passive margin stage in the south-central Andean region of the Gondwana margin (*e.g*., Bahlburg and Hervé, 1997; Cawood, 2005; Bahlburg *et al.*, 2009). This is supported by the absence or scarcity of Devonian detrital zircon grains along the proto-Andean margin from northern Peru to central Chile (*e.g*., Hervé *et al.*, 2013; Bahlburg *et al.*, 2009; Reimann *et al.*, 2010; Augustsson *et al.*, 2015; Einhorn *et al.*, 2015), and by the lack of evidence of coeval magmatism, deformation or metamorphism (Bahlburg and Hervé, 1997; Lucassen *et al.*, 2000; Chew *et al.*, 2007; Cardona *et al.*, 2009). Nevertheless, some authors suggested that the absence (or scarcity) of Devonian detrital zircons is a consequence of an inland (eastward) migration of the magmatic arc front during this period (*e.g*., Charrier *et al.*, 2007; Dahlquist *et al.*, 2018). These proposals, however, do not consider the tectonic and magmatic segmentation of the Gondwana margin (*e.g*., Calderón *et al*., 2020; Dahlquist *et al*., 2021; Creixell *et al*., 2025). Recently, Bahlburg (2022) proposed that there was an active margin here during the Devonian, and that the scarcity of Silurian- and Devonian-aged zircons is due to a decrease in magmatic activity (magmatic lull phase) during these periods.

The relation between the CLMC and the low-grade metasedimentary units of the late Palaeozoic Gondwana margin is unclear, as are the P-T metamorphic conditions of formation of the CLMC and the geodynamic implications of this process. There are also no accurate data on the timing of the deformation/metamorphism directly related to the 'Toco Orogeny'.

The aim of this paper is to determine and quantify the P-T conditions of formation of the migmatites of the CLMC, using thermodynamic calculations of mineral equilibrium (P-T pseudosections; Perple_X; Connolly, 2005) and geothermometers based on the mineral chemistry. New U-Pb detrital zircon ages and structural data were obtained in order to identify the protolith and the regional geological context of these rocks. Collectively, these findings help constrain the timing and nature of the 'Toco Orogeny', demonstrating its link with the development of the CLMC, and provide insights into the geodynamic evolution of the middle to late Palaeozoic proto-Pacific margin of Gondwana in this area.

2. Geological overview

Outcrops of Palaeozoic rocks in the Coastal Cordillera of northernmost Chile (18°30'-24°00' S) are very limited in comparison with those of Mesozoic

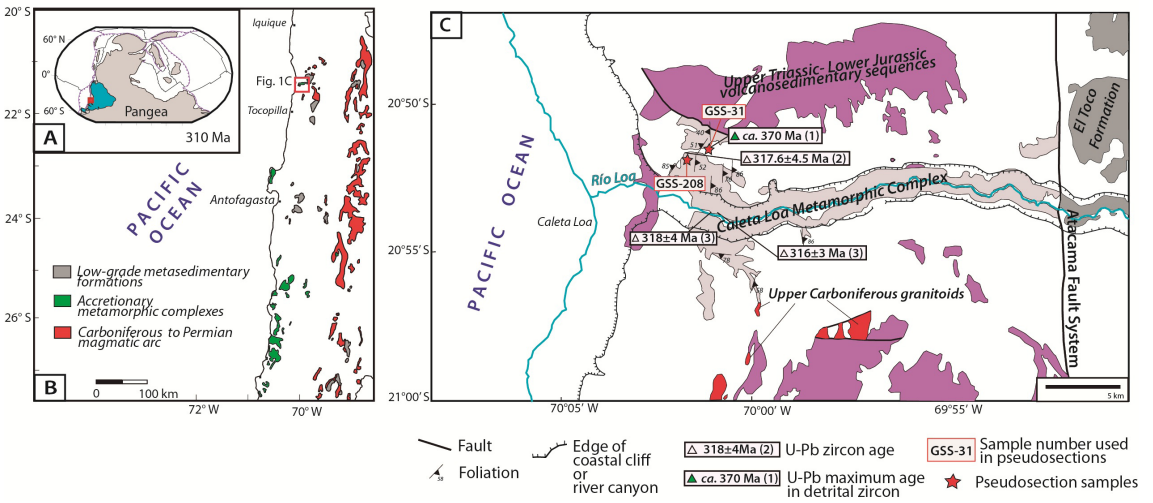

FIG. 1. **A.** Palaeographic reconstruction of Pangea at 310 Ma (Torsvik and Cocks, 2013). The red square shows the approximate location of panel B, and the cyan area refers to the South American continent. **B.** Location and regional geological context of upper Palaeozoic units (modified from Creixell *et al*., 2021). The red square indicates the location of the study region. **C.** Schematic geological map of the CLMC area (after Vásquez *et al.*, 2018). U-Pb zircon ages from: (1) this study, (2) Vásquez *et al*. (2018), and (3) Pankhurst *et al*. (2016).

rocks (Sernageomin, 2002). The former comprise a variety of low-grade deformed Upper Devonian to lowest Carboniferous metasedimentary units, Upper Carboniferous granitic plutonic rocks, and scarce migmatites of the same age. The metasedimentary units are the El Toco (Harrington, 1961) and the Sierra del Tigre (Niemeyer *et al.*, 1997) formations, which represent turbiditic marine deposits of the SW Gondwana margin (Bahlburg and Breitkreuz, 1993; Bahlburg and Hervé, 1997; Niemeyer *et al.*, 1997).

The restricted migmatite outcrops have been known since the early 1990s (cf. Lucassen *et al.*, 1994) and were lately defined as the CLMC by Vásquez *et al.* (2018). The rocks of the CLMC in the Río Loa canyon, near its mouth, were first described by Lucassen *et al.* (1994, 1996) and Wilke *et al.* (1997). They identified stromatic migmatites with sparse intercalations of equigranular gneisses, pegmatitic layers, and dioritic orthogneisses (amphibolites). Lucassen *et al.* (1996) determined peak metamorphic temperature conditions of 600-750 °C, and low-pressure conditions were suggested (Lucassen *et al.*, 1996, 2000; Wilke *et al.*, 1997).

Vásquez *et al.* (2018) showed that this complex extends continuously along the Río Loa canyon from near its mouth eastwards to the main trace of the Atacama Fault System (AFS; see Skarmeta and Marinovic, 1981), as well as in the hills adjacent to the canyon in the western part of the Coastal Cordillera (Figs. 1C and 2A). The base of the CLMC is not exposed. Its outcrops are covered by Upper Triassic-Lower Jurassic volcanic rocks and it is intruded by Upper Jurassic and Lower Cretaceous plutonic bodies. The AFS separates the CLMC from the El Toco Formation to the east (Fig. 1C). Vásquez *et al.* (2018) described the CLMC as mainly composed of stromatic metatexitic migmatites and diatexitic migmatites. However, the lithology of the CLMC is re-evaluated in this study, redefining it as composed of stromatic metatexitic migmatites and rare gneisses only, with predominant and continuous layer-parallel bands of leucosome at outcrop scale (see Fig. 2). Three samples of the CLMC previously yielded zircon U-Pb ages of *ca*. 318-316 Ma (Pankhurst *et al.*, 2016; Vásquez *et al.*, 2018), which were taken as the age of metamorphism and migmatite formation. Younger K-Ar biotite ages (*ca.* 189 and 170 Ma; Lucassen *et al.*, 2000) are interpreted as reset by Jurassic magmatic activity. The U-Pb zircon age patterns obtained by Pankhurst *et al*. (2016) are similar to those of local detrital samples (*e.g*., Sierra del Tigre Formation); together with the metamorphic mineral assemblages (see below), they indicate a sedimentary protolith for the migmatites of the CLMC.

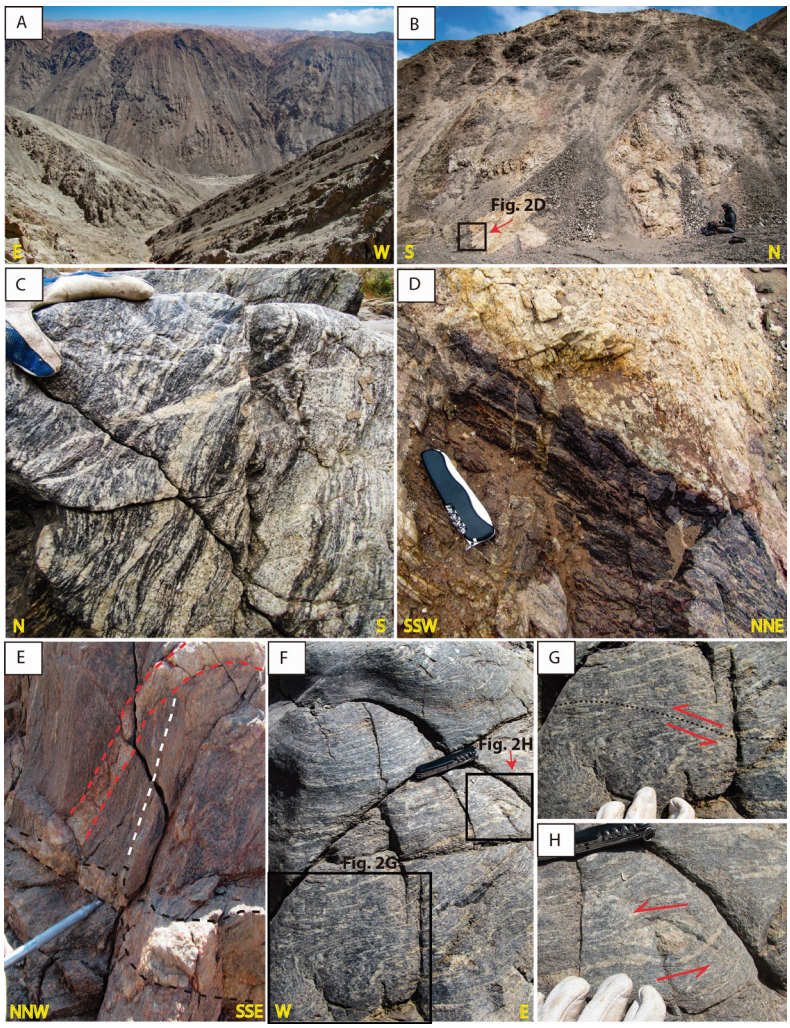

FIG. 2. Outcrop photographs of the CLMC. **A.** General view with the Río Loa at the bottom of the canyon. **B.** Metric-scale leucosome (whitish yellow to pale pink) emplaced in melanosome (dark grey). **C.** Average banded migmatite, with parallel coarse-grained leucocratic bands, as well as coeval melt-filled shear zone cutting the banding at low angle. **D.** Detailed view of B, showing subvertical veinlets of leucosome feeding the leucosome blob. **E.** Textural continuity between cross-cutting band (black dashed lines) and low-angle veins of leucosome (red dashed lines), with white dashed line showing the main foliation. **F.** Stromatic migmatite with top-to-the west shear indicators, including albite porphyroblast with sigma structure (right, centre) and folds associated with a low-angle shear zone (left, bottom). **G.** Detail of F showing shear zone and folds indicating top-to-the west thrusting (dashed black line). Note that folds are affected by S_2 foliation. **H.** Centimetric albite porphyroblast with sigma structure indicating top-to-the west sense of shear.

3. Methodology

Six rock samples from the melanosome of the CLMC were studied petrographically as summarised in Table 1. They were classified as biotite-gneiss (GSS-208, GSS-267), biotite-sillimanite gneiss (GSS-31), biotite-garnet gneiss (3/278, 3/347), and dioritic orthogneiss (3/276). Two of these (GSS-31 and GSS-208) were analysed for whole-rock geochemistry (Table 2), and five for mineral chemistry: two by scanning electron microscopy (SEM) with energy-dispersive spectroscopy (EDS) (GSS-31 and GSS-208; Supplementary Table 1) and five by electron probe microanalyzer (EPMA) (GSS-31, GSS-208, 3/276, 3/278, and 3/347; Supplementary Table 2). Analytical techniques are described in Appendix A.

TABLE 1. CLMC SAMPLES, LOCATIONS, MINERAL ASSEMBLAGES, AND METHODS APPLIED IN THIS STUDY.

Sample	UTM coordinates		Geographic coordinates		Metamorphic phases										Accesory phases		Pseudosections	Geothermometer	U-Pb dating
	E	N	W	S	Quartz	Plagioclase	K-felspar	Biotite	Sillimanite	Garnet	Cordierite	Ilmenite	Amphibole	Muscovite[1]	Chlorite[1]	F-Apatite	Monzonite		Ti in Biotite	
GSS-31	394,691	7,631,771	70°0'57''	21°24'47''	x	x	x	x	x			x		x			x	x	x	
GSS-208	394,209	7,631,272	70°1'14''	21°25'3''	x	x	x	x	x		x	x		x		x	x	x	x	
GSS-267	395,066	7,632,192	70°0'44''	21°24'34''	x	x	x	x				x		x						x
3/276(*)	397,780	7,629,614	69°59'11''	21°25'58''	x	x		x					x	x	x				x	
3/278(*)	397,772	7,629,516	69°59'11''	21°26'2''	x	x		x		x		x		x		x				
3/347(*)	397,587	7,629,534	69°59'17''	21°26'1''	x	x		x		x				x	x				x	

(*)approximate location
[1] retrograde phase

TABLE 2. WHOLE-ROCK AND MINERAL CHEMISTRY OF MIGMATITE SAMPLES FROM THE CLMC.

	Whole-rock composition		Representative mineral analyses*										
Sample	GSS-31	GSS-208	GSS-31							GSS-208			
Mineral phase (analysis n°)			Biotite (5)	Biotite (6)	White mica (4)	White mica (14)	Plagioclase (10)	Plagioclase (12)	Sillimanite (1)	Biotite (1)	White mica (5)[1]	White mica (6)[2]	Ilmenite (3)
SiO_2	71.22	73.90	34.39	34.57	44.25	45.02	62.57	60.17	36.83	34.96	46.37	46.81	0.00
Al_2O_3	12.58	12.11	19.77	8.13	35.38	36.25	23.01	24.98	62.46	19.24	35.86	36.18	0.24
TiO_2	0.97	0.82	2.59	2.94	0.21	1.19	0.02	0.01	0.01	1.85	0.30	0.01	56.67
FeO	-	-	20.06	20.39	1.03	0.74	0.07	0.07	0.17	21.03	0.80	1.69	34.59
Fe_2O_3	5.13	4.84	-	-	-	-	-	-	-	-	-	-	-
CaO	1.34	0.62	0.04	0.02	0.05	0.00	3.64	5.70	0.03	0.00	0.00	0.00	0.09
MgO	1.59	1.91	8.42	8.13	0.66	0.42	0.00	-	0.02	7.77	0.00	0.00	0.10
MnO	0.04	0.04	0.15	0.16	0.03	0.00	0.01	-	0.00	0.16	0.43	0.99	2.43
Na_2O	2.24	1.28	0.22	0.23	0.44	0.47	9.76	8.58	0.00	0.00	0.00	0.00	0.00
K_2O	2.08	2.98	9.02	9.19	10.50	10.02	0.09	0.14	0.20	9.24	9.91	8.42	0.27
P_2O_5	0.12	0.12	-	-	-	-	-	-	-	-	-	-	-
Total	97.30	98.62	94.66	95.29	92.55	94.11	99.15	99.66	99.71	94.66	93.67	94.10	94.77
Cations													
Si	-	-	5.287	5.291	3.034	3.020	2.791	2.688	0.998	5.419	3.106	3.105	0.039
Na	-	-	0.060	0.068	0.059	0.062	0.844	0.743	0.000	0.000	0.000	0.000	0.000
Ca	-	-	0.070	0.003	0.004	0.000	0.174	0.273	0.001	0.000	0.000	0.000	0.035
K	-	-	1.769	1.794	0.918	0.857	0.005	0.008	0.007	1.827	0.847	0.712	2.946
Fe	-	-	2.579	2.610	0.059	0.042	0.003	0.003	0.004	2.726	0.045	0.095	0.210
Mn	-	-	0.020	0.021	0.002	0.000	0.000	0.000	0.000	0.021	0.000	0.000	0.015
Mg	-	-	1.929	1.854	0.068	0.042	0.000	0.000	0.001	1.795	0.042	0.097	0.029
Al	-	-	3.583	3.547	2.860	2.866	1.210	1.315	1.996	3.516	2.831	2.828	4.340
Ti	-	-	0.299	0.338	0.011	0.060	0.001	0.000	0.000	0.215	0.015	0.001	7.624
Al^{IV}	-	-	2.713	2.709	0.966	0.981	-	-	-	-	0.894	0.895	-
Al^{VI}	-	-	0.870	0.839	1.894	1.885	-	-	-	-	1.937	1.932	-
F	-	-	-	-	-	-	-	-	-	-	-	-	0.010
Sum	-	-	15.544	15.526	7.015	6.947	5.028	5.030	3.007	15.512	6.886	6.838	15.248
Albite	-	-	-	-	-	-	83	73	-	-	-	-	-
Orthoclase							1	1					
Anorthite	-	-	-	-	-	-	16	26	-	-	-	-	-
Fe/(Fe+Mg)	-	-	0.572	0.585	-	-	-	-	-	0.603	-	-	-
Mg+Fe			-	-	0.127	0.084	-	-	-	-	0.087	0.192	-

All concentrations in wt%
* Cations calculated on the basis of: 22 oxygens (biotite), 11 oxygens (white mica), and 8 oxygen (plagioclase) in structural formulae
[1] muscovite analysis shows a deficit in the interlayer cations
[2] muscovite analysis shows that the sum of divalent cations (Mg+Fe) is too low for its Si content

3.1. Pseudosection modelling

In order to determine the P-T conditions of the CLMC, P-T pseudosections were constructed with the Perple_X software package (Connolly, 2005; version from September 2018 downloaded from http://www.perplex.ethz.ch/) using the bulk rock composition of samples GSS-31 and GSS-208 (Table 2). The metamorphic mineral assemblage of these samples is sillimanite+biotite+plagioclase +K-feldspar+quartz+cordierite+ilmenite (Table 1). Calculations were carried out in the Mn-Na-Ti-Ca-K-Fe-Mg-Al-Si-H-O system using the thermodynamic database of Holland and Powell (1998, updated in 2002) for minerals and H_2O (model CORK: Holland and Powell, 1991). A P-T range of 1-6 kbar and 500-800 °C was considered for the P-T pseudosections. After the construction of the pseudosections, they were contoured with isopleths for various modal (melt content) and chemical (*e.g*., Si content of white mica) parameters by applying the sub-programs *werami* and *pstable*. The final pseudosections and contoured P-T diagrams were redrawn by smoothing curves as demonstrated by Connolly (2005).

The following solid solution models (see Powell and Holland, 1999) compatible with this data set were selected: Gt(HP) for garnet, Bio(WPH) for biotite, IlGkPy for ilmenite, Pheng(HP) for white mica, Mica(M) for paragonite, hCrd for cordierite, feldspar for feldspars, Opx(HP) for orthopyroxene, Cpx(HP) for clinopyroxene, St(HP) for staurolite, Chl(HP) for chlorite, Ep(HP) for epidote, and GlTrTsPg for amphibole. For the silicate melt, the haplogranitic melt model melt (HP) was applied (White *et al.,* 2001). The fluid was considered to be pure H_2O.

The composition of the studied samples was modified to fit the 11-component system: P_2O_5 was fractionated as apatite, together with the corresponding amount of CaO. All Fe was considered as divalent, owing to the lack of Fe^{3+}-rich oxides and the negligible amount of Fe^{3+} in the analysed minerals. Oxygen content (O_2) was set to 0.02 for sample GSS-31 and neglected (O_2=0) for sample GSS-208, due to the absence of magnetite, the low amount of ferric iron in minerals, and the presence of ilmenite in the metamorphic association, which indicate low oxidation conditions (*e.g*., Diener and Powell, 2010). Different values of H_2O (between 1 and 4 wt%) and O_2 (0-0.05 wt%, maximum value corresponding to 10% Fe^{3+} of the total iron; see Massonne *et al.*, 2007) were considered during preliminary calculations. The variation of O_2 content resulted in minor changes of the pseudosections topology, with no significant changes in the considered phase-in boundaries. Most notable changes in these boundaries were related to variations in the amount of H_2O, such as the appearance of garnet below 500 °C at high pressures or above 650 °C at low pressures, or the existence of white mica at relatively high temperatures. For the final calculations, the water content was set to a maximum of 3 wt% to guarantee a free hydrous fluid phase. The melt volume was used to constrain the P-T conditions, with a maximum of 20 vol.%, which is near the upper limit defined for stromatic migmatites (White *et al.*, 2005; Sawyer, 2008), and agrees with our field observations.

Since uncertainties of 10% on the P- and 5% on the T-estimates resulting from pseudosection modelling have been reported (*e.g*., Massonne, 2013), our T data were compared with the temperature range obtained through Ti in biotite geothermometers.

3.2. Zircon U-Pb LA-ICP-MS geochronology

U-Pb isotopic composition of zircons from melanosome sample GSS-267 was obtained by LA-ICP-MS (laser ablation-inductively coupled-mass spectrometry) at the Isotopic Geology Laboratory of Sernageomin. The sample was crushed and pulverized in a Retsch pulverizer to ≤500 μm. Heavy mineral concentration was made using a Gemini table followed by hand-picking under UV lamp (Suárez *et al*., 2015). A random selection of 100 hand-picked zircon grains was mounted for polishing on a 2.5 cm diameter epoxy resin disc together with Temora-2 standard zircon (Black *et al.*, 2004). Cathodoluminescence (CL) SEM images were obtained using a Zeiss MA-10 Scanning Electronic Microscope, with a Gatan ChromaCL2 UV CL detector and a Zeiss annular BSE (backscattered electron) detector. Zircon grains were ablated using a Photon Machines Analyte G2 193 nm ArF (Argon Fluoride) excimer ablation system coupled to a Thermo Scientific Element XR ICP-MS system with the following parameters: 30 μm beam size, 10 Hz repetition rate, and a beam energy density of 6 J/cm^2. The depth of each ablation pit was 15-20 microns. U, Pb, and Th concentrations were calculated relative to the reference zircon GJ-1 (Jackson *et al.,* 2004). Following baseline correction, the Pb/U ratios were corrected for downhole fractionation and normalized to reference zircon GJ-1. The data were reduced following procedures given in

Williams (1998) using the Iolite software (Petrus and Kamber, 2012). Probability density and Concordia plots were carried out using the Isoplot macro (Ludwig, 2012). $^{206}Pb/^{238}U$ ages were corrected for common Pb by using measured ^{207}Pb (Williams, 1998). Radial plots and Maximum Likelihood Age (MLA; Vermeesch, 2021) were calculated with IsoplotR (Vermeesch, 2018). Reported uncertainties were always given at the 2σ level.

4. Results

4.1. Lithological and structural features

The leucosome is present as layer-parallel bands, dykes, sills, and veins, and metric-scale blobs (Fig. 2B-E). The layer-parallel bands are fine- to coarse-grained, and their thickness is irregular, varying between 0.2 to 10.0 cm, defining a compositional banding foliation (Fig. 2C, F). At outcrop scale, the contacts between these leucosome bands and the melanosome are diffused to stepped, locally sharp (*sensu* Pawley *et al.*, 2015). Leucosome dykes, sills and veins are discontinuously distributed within the metamorphic complex, varying in thickness from a few centimetres up to decimetres. In general, they have sharp stepped margins, with scarce cases of a sharp straight-edged margin. In some cases, dykes and sills have a millimetric biotite-rich narrow selvedge, suggesting late melting. Locally, in the upper sections of the Río Loa canyon, the dykes fed metric scale leucosome bodies. The dykes cut the melanosome at moderate to high angles (~45°-90°; Fig. 2D, E). The modal composition of the coarse-grained leucosome corresponds to granite with variable proportions of biotite (1-5%) and muscovite (1-3%), whereas rare metric leucosome bodies correspond to biotite-muscovite-garnet granite (5% garnet). As no occurrences of leucosome have been observed outside the metamorphic complex, it has been classified as *in situ* and in-source leucosome (*sensu* Sawyer, 2008). The melanosome occurs as highly deformed, dark biotite-rich domains with sub-millimetric to millimetric granoblastic domains. The lepidoblastic domain includes sillimanite, ilmenite and scarce cordierite, as well as white mica replacing former biotite and sillimanite.

The foliation (S_1) in the CLMC is orientated mainly N-S, with 20° to 86° E dips. E-W and NNE-SSW strike variations are also observed, with 5° to 60° N to NW dips. Locally, the foliation is affected by discrete low-angle, occasionally melt-filled, reverse shear bands (Fig. 2C, F, G; Appendix B). These bands generated upright, moderately inclined to recumbent folds, of centimetric to decametric scale, whose axial planes generally trend N-S and dip 5° to 50° E, indicating westward vergence. Late leucosome sills, with mafic selvedge, are also affected by this folding. Occasionally, these folds exhibit an S_2 foliation that is parallel or at a low angle (<30°) to the S_1 (locally transposed) foliation (Fig. 2G; Appendix B). Blobs of leucosome were observed at the hinge of folds and other similar dilatational sites. Syn-tectonic feldspar porphyroblasts with pressure shadows also indicate a top-to-the west sense of shear (Fig. 2F, H; Appendix B).

4.2. Petrographical characteristics

Thirty thin sections with leucosome and melanosome in the same proportion were examined. In the melanosome, the foliation is parallel spaced and locally anastomosed, defined by grano-lepidoblastic levels formed by biotite (85-90%), white mica (0-10%), and rare sillimanite bundles (fibrolite; <5%) (Fig. 3A, B). Biotite and white mica crystals display kink-bands. Irregular-shaped to elongated grains of quartz, with less plagioclase, K-feldspar, and scarce altered cordierite (<2%) are also present. Biotite and white mica occur with a preferred orientation within leucocratic granoblastic pods in the melanosome among anhedral quartz, plagioclase and K-feldspar crystals. Aggregates of biotite, white mica and ilmenite intergrowths are observed as well. Quartz and/or plagioclase porphyroblasts develop sigma-type structures of fine-grained quartz and white mica, indicating a sinistral (top-to-the west) sense of shear.

Leucosome layers parallel to the main foliation are made up of quartz (50-80%), plagioclase (10-30%) and K-feldspar (locally microcline) (10-15%), with minor (≤5%) biotite and white mica. The granoblastic crystals exhibit serrated to lobate grain boundaries and quartz shows undulose extinction (locally chessboard extinction), suggesting deformation, dynamic recovery, and grain boundary migration during recrystallisation. Biotite and white mica crystals also display kink-bands. Plagioclase locally shows secondary white mica growing along its cleavages, whereas K-feldspar is highly altered to sericite, and biotite to chlorite, with sericite-filled fractures cutting the foliation.

Two samples (3/278 and 3/347) show garnet and biotite porphyroblasts in a matrix of plagioclase, quartz,

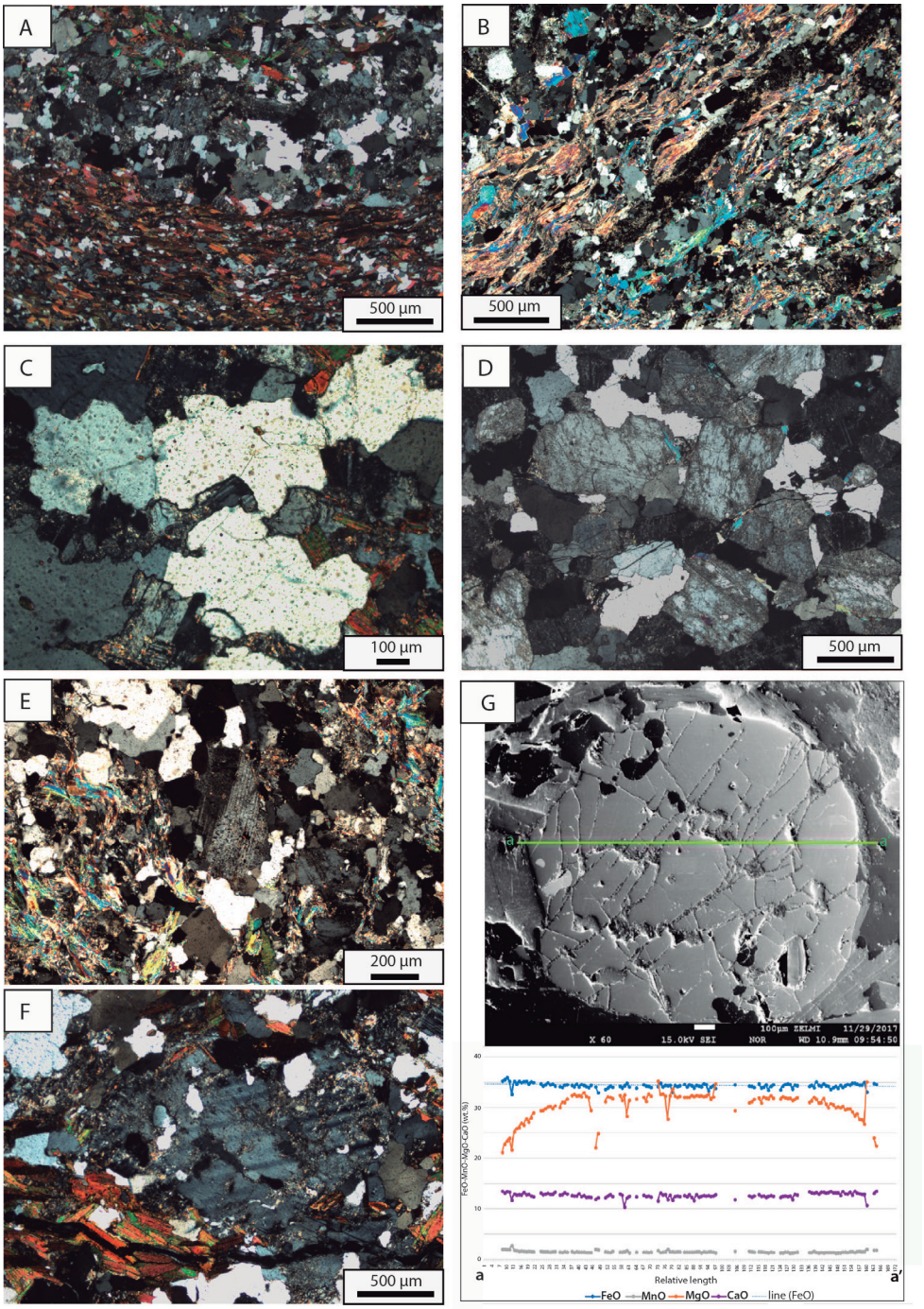

FIG. 3. Representative thin sections (**A-F**) and BSE image (**G**) of the CLMC. **A.** General view of lepidogranoblastic domains with biotite defining the foliation and typical lobated textures of mineral grains (sample GSS-185, crossed polars). **B.** Anastomosing foliation with muscovite replacing sillimanite (fibrolite) crystals (sample PPV-14, crossed polars). **C.** Details of "branching" plagioclase in quartz, together with lobate textures (sample GSS-185, crossed polars). **D.** Typical granitic leucosome, with interstitial muscovite, branching K-feldspar (top to the right), and cuspate quartz with low dihedral angle (right in centre) (sample GSS-197, crossed polars). **E.** Deformation twins in plagioclase and string of beads (centre-right) (sample PPV-14, crossed polars). **F.** Corroded plagioclase crystal (sample GSS-185, crossed polars). **G.** BSE image of garnet (sample 3/278), showing element distribution (in wt%) along the profile *a-a'*.

biotite and white mica, suggesting distinctive paleosome composition. The garnet crystals have predominant almandine composition (see Supplementary Table 2), are ~2.0-2.5 mm in size and partly idiomorphic, exhibiting numerous inclusions of biotite and retrograde chlorite at the edges and along cracks.

In cleavages and/or at chlorite alteration zones, biotite crystals exhibit sagenitic rutile crystals. Ilmenite is the stable Ti-rich phase, generally occurring disseminated with a preferred orientation. Accessory phases are apatite, monazite, zircon and graphite.

Several microstructures indicate that samples underwent melting processes (see Holness *et al.*, 2011): 1) undulose (locally chessboard) extinction of quartz and irregular to lobate grain boundaries of quartz and plagioclase (Fig. 3A, C); 2) films and "branching" grains of K-feldspar between quartz crystals (Fig. 3D); 3) isolated faceted grain boundaries of plagioclase; 4) cuspate low dihedral angles in quartz crystals (Fig. 3D) ; 5) "string of beads" of quartz (Fig. 3E); and 6) corroded quartz and plagioclase grains (Fig. 3F)

The inferred peak metamorphic mineral assemblage is considered to have been sillimanite+biotite +plagioclase+K-feldspar+quartz+cordierite+ilmenite (+melt), whereas for garnet-bearing samples the peak metamorphic assemblage is garnet+biotite+plagioclase +quartz+ilmenite (+melt) (Table 1). White mica (muscovite, see below) is considered a post-peak phase developed during subsequent decompression and/or cooling. White mica in fractures and in cleavages and chlorite suggests very late fluid infiltration.

4.3. Mineral chemistry

Five migmatite samples were chosen for mineral chemistry (GSS-31, GSS-208, 3/276, 3/278 and 3/347; Hemmelmann, 2018). Representative EPMA analyses of two samples (GSS-31 and GSS-208) for which pseudosections were elaborated are presented in table 2. The rest of the analyses are available in Supplementary Table 2.

Muscovite was analysed in samples GSS-31, GSS-208 and 3/276. The content of Si varies between 3.00 and 3.11 per formula unit (pfu), X_{Mg} = 0.43-0.56, and Ti contents as high as 0.07 pfu.

Garnet in samples 3/278 and 3/347 is mainly almandine (74-80 vol.%), with 10-18 vol.% pyrope, 4-7 vol.% grossular and 3-5 vol.% spessartine. X_{Mg} is less than 0.2, with higher values in cores. In sample 3/278, the proportion of almandine is 76-80%, whereas in sample 3/347 is 74-77%. The absence of zonation in the core of the crystals suggests chemical diffusion processes, whereas the strong decrease in MgO at the rim is indicative of retrograde metamorphism (see Fig. 3G).

Biotite crystals show similar compositions in all analysed samples, though biotite inclusions in garnet (samples 3/278 and 3/347) have lower Mg and higher Ti contents, and biotite from sample GSS-31 is richer in Mg. On the basis of 22 oxygen atoms in the structural formula, the biotite composition is defined by: Si= 5.286-5.730 pfu, X_{Mg}=0.36-0.46, and Ti=0.0-0.53 pfu. Sample 3/347 is strongly chloritized.

The composition of plagioclase varies notably among samples: plagioclase from sample GSS-31 is oligoclase (An17-An27), in sample 3/347 the composition is An48-An51, and sample 3/276 contains labradorite (An49-An60) and bytownite (An81-An86), with centres of almost pure anorthite.

Amphibole is present only in sample 3/276 and is grunerite (after Hawthorne *et al.*, 2012), with Si = 7.76-7.84 pfu, Al_{IV} = 0.16-0.24, Fe=3.44-3.55 pfu, X_{Mg} = 0.47-0.48, Ti = 0.01, and Na = 0.03-0.06 pfu.

Ilmenite was analysed in sample GSS-208, showing a Mn content of 0.21 pfu. In general, it is present as fine elongated crystals within the cleavage of biotite. Sillimanite and monazite (samples GSS-31 and GSS-208), cordierite (sample GSS-208) and F-apatite (samples GSS-208 and 3/278) were observed as well.

4.4. Geothermometry

Ti-in-biotite geothermometry was performed on samples 3/347, 3/276, GSS-208, and GSS-31 (Table 1), applying the calibrations of Henry *et al.* (2005) and Wu and Chen (2015). The pressure for the Wu and Chen (2015) geothermometer was set to 0.4 GPa based on the preliminary results from pseudosections (see below). This geothermometer is optimised for ilmenite- and/or rutile-bearing samples, making it suitable for the selected samples. All Fe was considered to be divalent, based on the lack of Fe^{3+} bearing phases. Temperatures obtained for sample 3/347 are 663-728 °C (mean=686 °C) using the geothermometer of Henry *et al.* (2005), and 606-702 °C (mean=654 °C) using the method of Wu and Chen (2015). For sample 3/276, the equivalent results are 655 °C and 577 °C, respectively, for sample GSS-208 they are 581 °C and 583 °C, and for sample GSS-31 they fluctuate between 600 and 666 °C (mean=638 °C) and 566

and 642 °C (mean=608 °C). It is noteworthy that the application of the geothermometer of Henry *et al.* (2005) yielded systematically higher temperatures (up to 78 °C) than those using Wu and Chen (2015) (see Supplementary Table 2). Sagenitic rutile and/or chlorite within biotite crystals were observed in several thin sections, indicating retrograde mineral reactions. According to Henry *et al.* (2005), in these cases, the application of Ti-in-biotite geothermometers could result in anomalously low temperature estimates compared to other geothermometers. Nevertheless, the temperatures obtained here using this method are only slightly lower than those calculated using pseudosections (see below).

4.5. Pseudosection modelling and P-T constraints

The P-T pseudosections for GSS-31 and GSS-208 are shown in figures 4 and 5. P-T conditions were derived by projecting the XFe=Fe/(Fe+Mg) isopleth of biotite onto the P-T field of the peak metamorphic mineral assemblage and intersecting it with the melt content within the same P-T field. The Si isopleths of muscovite were also calculated, but

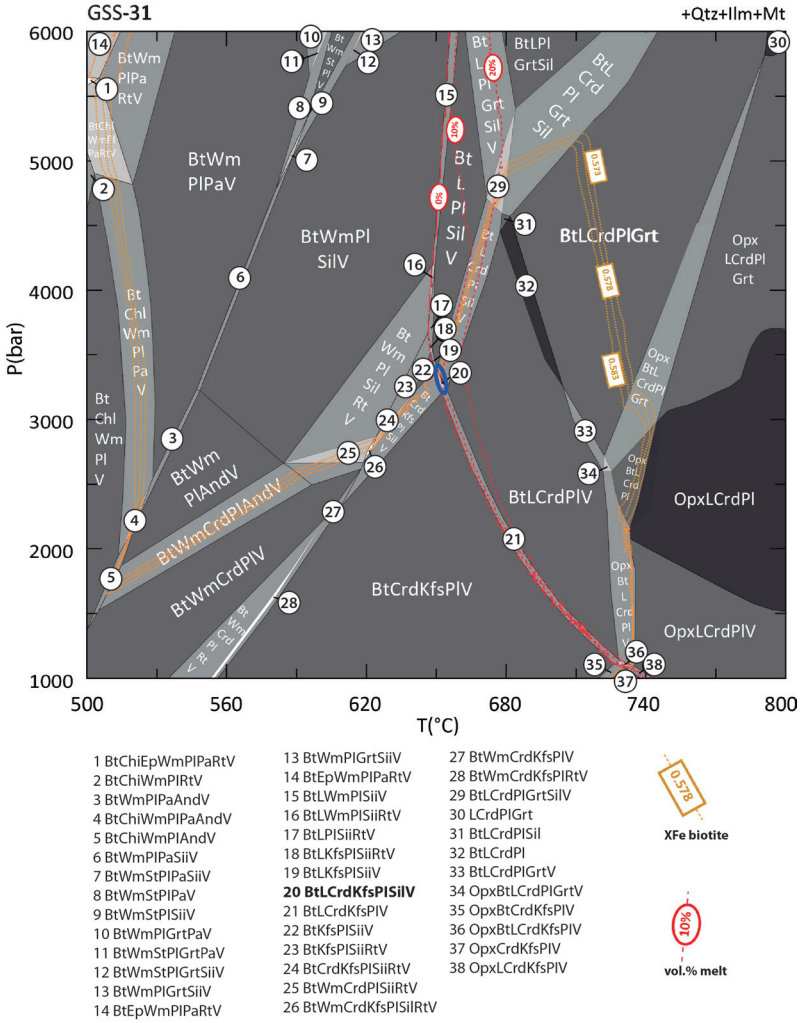

FIG. 4. Pseudosection of sample GSS-31. Peak metamorphic assemblage in bold letters. Blue ellipse marks the peak P-T conditions. Red segmented lines represent the calculated vol.% of melt. Orange dotted lines represent the XFe of biotite. Shading indicates degree of variance: white, divariant; light grey, trivariant; medium grey, quadrivariant; dark grey: quintvariant. **And:** andalusite, **Bt:** biotite, **Chl:** chlorite, **Crd:** cordierite, **Ep:** epidote, **Grt:** garnet, **Ilm:** ilmenite, **Kfs:** K-feldspar; **L:** melt, **Mt:** magnetite, **Opx:** orthopyroxene, **Pa:** paragonite, **Pl:** plagioclase, **Qtz:** quartz, **Sill:** sillimanite, **St:** staurolite, **Ru:** rutile, **V:** H_2O, and **Wm:** muscovite.

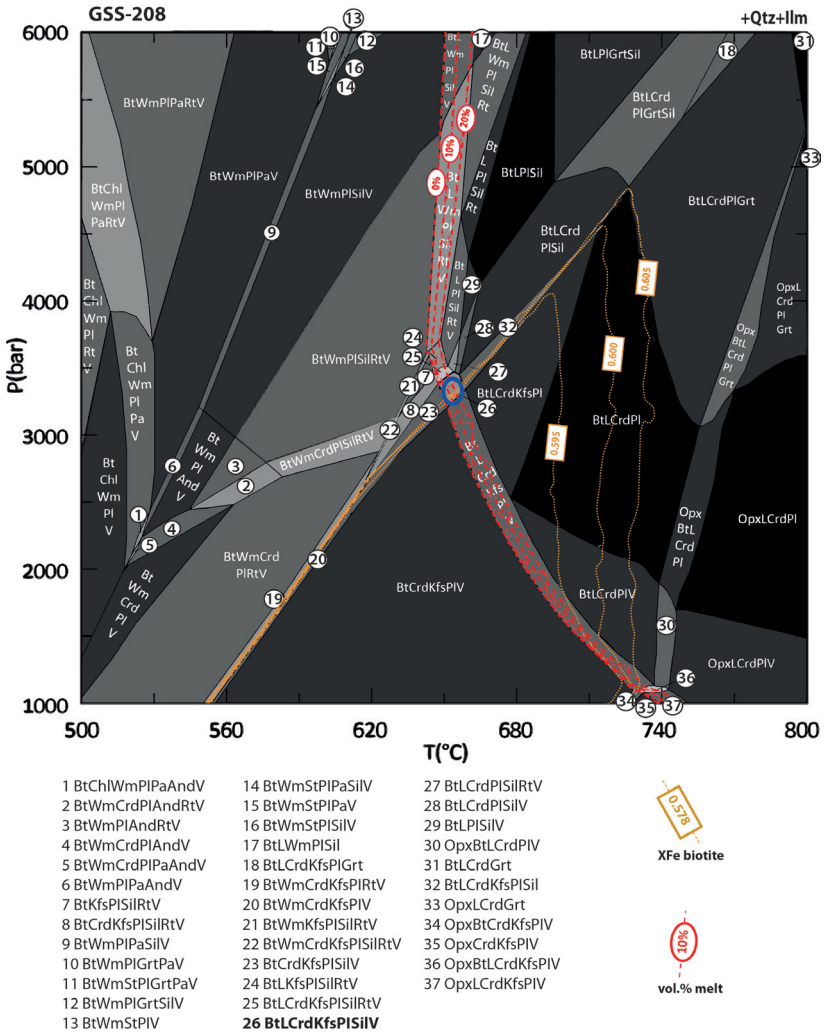

FIG. 5. Pseudosection of sample GSS-208. Peak metamorphic assemblage in bold letters. Blue ellipse marks the peak P-T conditions. Red segmented lines represent the calculated vol.% of melt. Orange lines represent the XFe of biotite. Shading and mineral abbreviations as in figure 4. Black shading: sextivariant.

the analysed Si content lied outside the P-T field of the peak metamorphic mineral assemblage, showing that it is a retrograde phase (see below).

For sample GSS-31 (Fig. 4), the XFe isopleth of biotite with the observed XFe content (mean=0.57 pfu) projects very close to the limit of the P-T field of the peak metamorphic mineral assemblage in this sample (biotite+sillimanite +quartz+albite+K-feldspar+ilmenite), within a contiguous field containing additional cordierite. The amount of cordierite in this P-T field is <5%, so it is probable that this mineral is present in the sample in very low amounts, which is supported by its presence in sample GSS-208 (Table 1). The intersection of the observed XFe content in biotite with this P-T field gives a range of about 3.35-3.40 kbar and 650-655 °C. The isopleths of ~10% melt also plot in the same P-T field. Moreover, the calculated plagioclase composition in the P-T field of the observed assemblage matches the observed composition (Ab72-Ab73). On the other side, the Si isopleth of muscovite from sample GSS-31 with the observed Si content (mean=3.02 pfu) lies below 1.8 kbar at ~480–550 °C, *i.e.*,

lower P-T conditions than those determined for the P-T field of the observed mineral assemblage, which indicates that the analysed crystals grew under retrograde metamorphism or hydrothermal alteration, as noticed in the petrographic analysis. Due to the election of O_2>0 in the calculations for this sample, magnetite is ubiquitous across all the P-T ranges, but always below 0.16%.

For sample GSS-208 (Fig. 5), the XFe isopleth of biotite matches the analysed XFe (~0.6 pfu) inside the P-T field of the observed mineral assemblage, at around 3.3-3.4 kbar and 640-650 °C, implying equilibrium. The isopleths of melt (10-20%) intersect the XFe isopleths of biotite on a narrow strip within the P-T field of the observed mineral assemblage, which yields a restricted P-T range of 3.30-3.35 kbar and 645 °C. On the other hand, two chemical analyses of muscovite did not provide proper stoichiometric results to estimate the P conditions (see Table 2).

In both pseudosections, the garnet stability is limited to higher temperatures (>680 °C) and/or higher pressures (P>4.5 kbar) (see figures 4 and 5).

4.6. Geochronology

A sample of the melanosome of the CLMC (sample GSS-267) was analysed by LA-ICP-MS U-Pb on inherited detrital zircons (Fig. 6A-C). The sample was collected from an outcrop near where sample GSS-31 was taken, and consists mainly of biotite, quartz, plagioclase, K-feldspar, and muscovite, with ilmenite, zircon and apatite as accessories (Table 1). In general, zircon grains are elongated with rounded to subrounded edges, with a few with angular edges. They display complex internal zoning at the CL images (Fig. 6B). All 100 zircon grains analysed were included in the results (see Supplementary Table 3). Th/U ratios are between 0.08 and 5.27, generally indicative of igneous zircons from multiple sources. The apparent ages range from *ca*. 368 to 2625 Ma. The youngest peak in the age pattern is *ca.* 450 Ma; there is also a significant grouping at 470 Ma and two prominent older peaks at 1050 Ma and 1350 Ma (Fig. 6A). The Maximum Likelihood Age (MLA; Vermeesch, 2021) is *ca*. 369±10 Ma (Supplementary Table 3), interpreted here as the oldest possible sedimentation age of the protolith of these metamorphic rocks.

5. Discussion

5.1. P-T conditions

The peak of metamorphism of the CLMC was attained at ~3.3-3.4 kbar and ~650 °C, under upper amphibolite facies conditions, implying a low P/T gradient. The temperatures determined by pseudosections agree with those obtained using other geothermometers (Ti-in-biotite), as well as being within the range of 600-750 °C reported by Lucassen *et al.* (1996) using an unspecified garnet-biotite geothermometer. Our pressure determination is in line with the observations of Lucassen *et al.* (1996, 1999, 2000), who indicated regional low-P metamorphic conditions due to the absence or minor presence of garnet. Assuming an average upper crustal density of 2,700 kg/m^3 (*e.g.*, Lucassen *et al*., 2001), a depth of ~13 km and a high geothermal gradient of ~52 °C/km can be derived from calculated metamorphic pressure conditions.

The presence of garnet in migmatite samples 3/278 and 3/347 suggests that this phase is either a remnant from an earlier stage of migmatisation at slightly higher P, or metamorphism of a paleosome with a composition different to that of the surrounding rocks. If garnet did grow before the observed mineral assemblage reached equilibrium at 3.3-3.4 kbar and 650 °C, the calculated P range would be a minimum. The occurrence of garnet in isolated leucosome outcrops could indicate growth under peritectic conditions (*e.g.*, Stevens *et al*., 2007), which would support this interpretation. However, a local particular paleosome richer in Fe than that of the samples used in the pseudosections cannot be ruled out, which would be necessary to equilibrate almandine garnet at P similar to that obtained by the pseudosections.

The pressure deduced from the Si content of muscovite (sample GSS-31) is below 1.8 kbar and outside the peak P-T range. Considering that the CLMC was already exhumed by the Late Triassic, this pressure could be attributed either to a retrograde reaction after the metamorphic peak, or to low-grade alteration associated with granitic intrusions that crop out in the Coastal Cordillera in the vicinity of the study area (Sepúlveda *et al.*, 2014; Vásquez *et al.*, 2018) (Fig. 1C), and were part of the extensive Late Carboniferous-Early Permian igneous activity (310-260 Ma, Maksaev *et al.*, 2014).

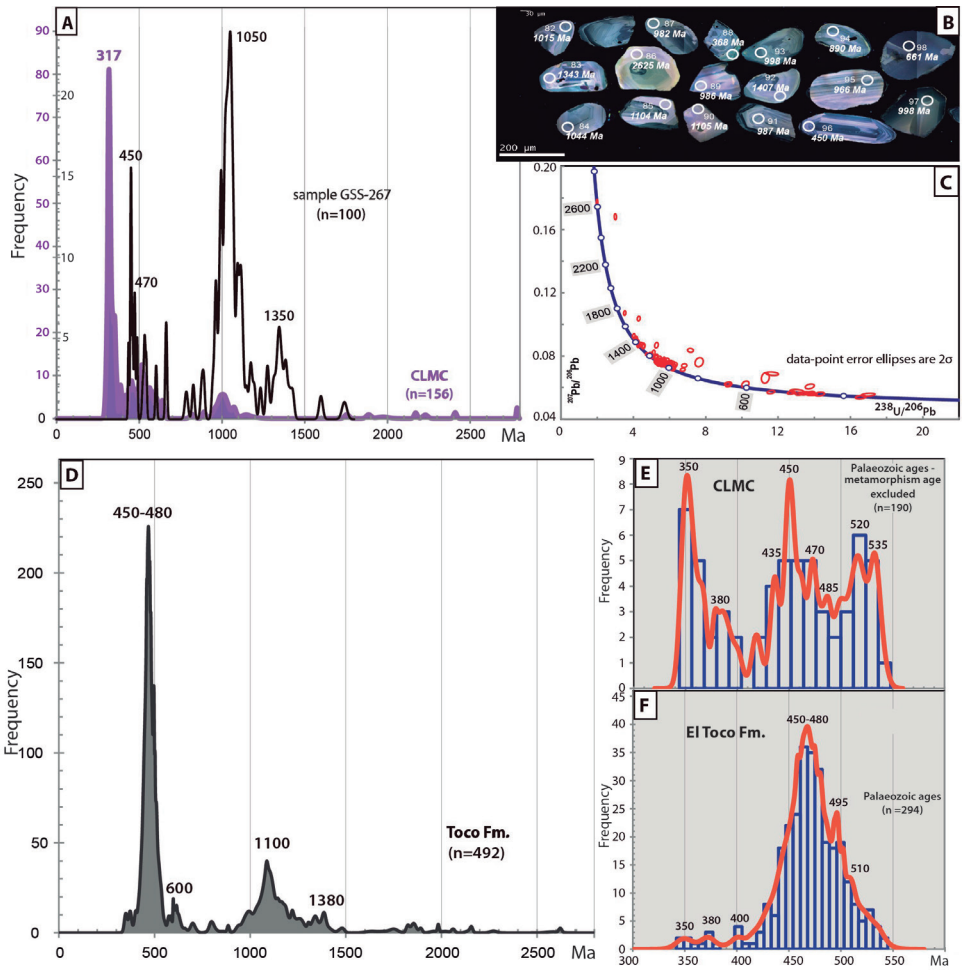

FIG. 6. **A.** Probability density plots with age histogram showing U-Pb zircon age distribution of sample GSS-267 (black line) and composite U-Pb zircon age distribution of the CLMC (purple), including data from Pankhurst *et al.* (2016) and Vásquez *et al.* (2018). **B.** Illustrative CL images of dated zircon grains (U-Pb ages in italics, below the zircon grain number) from sample GSS-267. **C.** Tera-Wasserburg plots of uncorrected U-Pb data for sample GSS-267. **D.** Composite U-Pb zircon age distribution of the El Toco Formation, based on literature data (Bahlburg *et al.,* 2009; Augustsson *et al.,* 2015; Einhorn *et al.,* 2015). **E.** Composite U-Pb zircon age distribution of Palaeozoic ages (<539 Ma) from the CLMC, excluding ages for metamorphism of this complex. **F.** Composite U-Pb zircon age distribution of Palaeozoic ages (<539 Ma) from the El Toco Formation. Age scale in E as in F.

The P-T conditions determined here strongly contrast with those inferred for the late Palaeozoic forearc metasedimentary units of the SW Gondwana margin in the Coastal Cordillera of northern Chile (18-24° S). The latter are deformed, low-grade sedimentary rocks (*e.g.*, Bahlburg and Breitkreuz, 1991), with metamorphic paragenesis that includes chlorite, white mica, albite and quartz (*e.g.*, Bobenrieth, 1980; Skarmeta and Marinovic, 1981; Bahlburg, 1987a; Niemeyer *et al.*, 1997).

5.2. Protolith of the CLMC

The two most prominent older peaks of the U-Pb detrital zircon age pattern of sample GSS-267 (1050 and 1350 Ma; Fig. 6A) are similar to the main Mesoproterozoic age components in the protolith of the Sierra de Moreno Metamorphic Complex (Aguilef *et al.*, 2019), a migmatite-bearing unit that forms the Precambrian to early Palaeozoic basement of the Precordillera at the same latitude.

This unit has traditionally been considered as part of the basement of the Antofalla crustal block (*e.g*., Loewy *et al.*, 2004; Ramos, 2008, 2010), where U-Pb detrital zircon age populations have been determined for the sedimentary protolith of the migmatites at *ca.* 1250 and 1200 Ma (Damm *et al.*, 1990), *ca.* 1025, 1140, 1170, and 1460 Ma (Pankhurst *et al.*, 2016), *ca.* 1000, 1060, and 1180 Ma (Aguilef *et al.*, 2019), and *ca.* 1050 and 1160 Ma (Sepúlveda *et al.*, 2024).

The Palaeozoic zircon ages show significant clusters at *ca.* 450 and 470 Ma (Fig. 6A, E). These ages were identified in the detrital zircon age pattern of the samples from the CLMC analysed by Pankhurst *et al.* (2016), as well as in the neighbouring El Toco and Sierra del Tigre formations (Bahlburg *et al.*, 2009; Augustsson *et al.*, 2015; Einhorn *et al.*, 2015, Pankhurst *et al.*, 2016; Antofagasta Minerals *in* Baeza and Astudillo, 2019). These ages are ubiquitous in all late Palaeozoic metasedimentary units in northern Chile (see Bahlburg *et al.,* 2009; Pankhurst *et al*., 2016; Creixell *et al.*, 2021) and represent the magmatic products of the Famatinian continental arc (Pankhurst *et al*., 1998; Ramos, 2008; Rapela *et al.*, 2018).

When the Early Pennsylvanian ages representing migmatite formation (*ca.* 318-316 Ma; Pankhurst *et al.*, 2016; Vásquez *et al.*, 2018) are filtered out, the Palaeozoic U-Pb detrital zircon age patterns of the CLMC exhibit a prominent peak at *ca.* 350 Ma (Early Mississippian), as well as a lesser peak at *ca*. 380 Ma (Late Devonian) (Fig. 6E). Therefore, the maximum depositional age of the protolith of CLMC is restricted to the Early Mississippian (*ca*. 350 Ma), which is even younger than the Maximum Likelihood Age (MLA, *ca*. 370 Ma) calculated for the sample of the CLMC analysed in this study.

A cluster at *ca*. 350 Ma was also identified in the U-Pb detrital zircon data from a sample of the El Toco Formation (Augustsson *et al*., 2015). The composite U-Pb detrital zircon age pattern of this unit (Fig. 6F) shows a Late Devonian peak (*ca*. 380 Ma). The Early Carboniferous maximum depositional age contrasts with the Upper Devonian biostratigraphic age of this unit (based on the presence of plant fossils; Moisan *et al*., 2011). Notably, both the geochronological and the fossil samples were collected from the same locality (Cerro Puntillas: 21°58' S; 69°47' W).

Late Devonian (*ca*. 370 Ma) and Early to Middle Mississippian (*ca*. 350, 344, and 335 Ma) maximum depositional ages have been determined in the Sierra del Tigre Formation (Antofagasta Minerals *in* Baeza and Astudillo, 2019), which are coherent with the maximum depositional age of *ca*. 380 Ma (MLA; Supplementary Table 4) calculated in this study for the sample of this unit analysed by Augustsson *et al*. (2015). There are no reports of plant fossils in the Sierra del Tigre Formation. Its age was initially assumed as Devonian sustained on an incomplete brachiopod fossil, tentatively assigned to *Mucrospirifer*(?) sp. (V. Covacevich *in* Ferraris and Di Biase, 1978), and later supported by lithostratigraphic correlation with the El Toco Formation (Niemeyer *et al*., 1997). However, the biostratigraphic range of the *Mucrospirifer* genus now extends into the Early Mississippian (Chen, 2010; Chen and Qing, 2024).

Despite the current inconsistencies between maximum depositional ages and biostratigraphic ages, the similarities between the Palaeozoic peaks in the U-Pb detrital zircon patterns of the CLMC and the El Toco Formation (and its southern equivalent, the Sierra del Tigre Formation) (Fig. 6A, D), together with the proximity of their outcrops (separated only by the main trace of the AFS; see Fig. 1C), allow us to infer that the protolith of the CLMC consisted of rocks of the El Toco Formation that were migmatised at upper crustal depths (~13 km) during the Early Pennsylvanian.

The Early Mississippian (*ca.* 350 Ma) age population marks the onset of the late Palaeozoic magmatic arc (*e.g*., Creixell *et al.*, 2021) or the Gondwanide magmatic flare-up (Bahlburg, 2022). In contrast, age clusters at *ca.* 370-380 Ma in the detrital zircon age distribution of the CLMC indicate the existence of a yet unrevealed Late Devonian magmatic source, whose products are also evident in the U-Pb detrital zircon data of the Devonian-Carboniferous Zorritas and Sierra de Argomedo formations (Augustsson *et al*., 2015). In this context, a Devonian-Carboniferous active margin setting has recently been argued for SW Gondwana by Bahlburg (2022) and García Zavaleta *et al.* (2024). The latter authors inferred a shift from flat-slab subduction during the Devonian to normal subduction in the Carboniferous. Although scarce, Devonian detrital zircons have also been reported farther east, in the late Palaeozoic Tarija Basin of southern Bolivia (22° S) by Calle *et al.* (2023) and Ferroni *et al.* (2025), indicating the presence of a magmatic source that fed this foreland basin from the west. Dahlquist

et al. (2021, and references therein) also proposed the existence of a Devonian calc-alkaline magmatic arc in the Frontal Cordillera of Argentina, albeit south of our study area (27°-35° S) and in a different segment of the SW Gondwana margin (*e.g*., Creixell *et al.*, 2025) with distinctive geodynamic events, including the accretion of the Chilenia microplate (*e.g*., Ramos *et al.*, 1986; Ramos, 2010; Boedo *et al*., 2016).

5.3. Structural contact between the CLMC and the El Toco Formation

Given that the El Toco and Sierra del Tigre formations are low-grade metasedimentary rocks (Bobenrieth, 1980; Breitkreuz and Bahlburg, 1985; Bahlburg *et al.*, 1987b; Niemeyer *et al.*, 1997; Vásquez *et al.*, 2018), the contrasting higher metamorphic P-T conditions of the CLMC imply that the contact between them is a major structural discontinuity, which uplifted the western block (CLMC) relative to the eastern block (El Toco Formation). The timing of its activity is constrained by the deposition of the Sierra de Lagunas Beds (Sepúlveda *et al.*, 2014), a Rhaetian-Pliensbachian volcano-sedimentary unit that unconformably covers both the CLMC and the El Toco Formation, sealing the structure between them. Later, this major structure was reactivated and incorporated as part of the main trace of the AFS during the Early Cretaceous (*e.g*., Scheuber and González, 1999; Grocott and Taylor, 2002).

5.4. Regional implications and tectonic event

The migmatisation event of the CLMC (*ca.* 318-316 Ma) forms part of a well-defined period of magmatism in Late Mississippian-Early Pennsylvanian times at the SW Gondwana margin (Maksaev *et al.*, 2014). Magmatism contemporaneous with migmatisation was recorded in the Precordillera, at nearly the same latitude, by Aguilef *et al.* (2018) and Dahlström *et al.* (2022), who obtained LA-ICP-MS U-Pb zircon ages of 316-310 Ma and *ca.* 315 Ma, respectively. Dahlström *et al.* (2022) determined an emplacement pressure of ~3.2 kbar for the same dated body (a hornblende-bearing granodiorite), similar to that obtained here for the CLMC migmatites (~3.3-3.4 kbar). In contrast, the pressure of emplacement determined by the same authors for many other younger intrusive bodies, from latest Carboniferous to late Eocene in age, was only ~1.2-1.9 kbar. The congruence of age and pressure (depth) of emplacement between migmatites and coeval intrusives, as opposed to emplacement conditions for younger plutonic bodies, suggests that the former shared a geodynamic/tectonic scenario where anatexis/magmatism occurred at deeper crustal levels. Further studies are required to establish whether the coeval high-T event and magmatism at 318-310 Ma (middle Carboniferous) in both the Coastal Cordillera and the Precordillera originated in the same magmatic arc, or they represent independent coeval events from different tectonic settings in the Gondwana margin. The first scenario would imply that the CLMC was part of the 'migmatite front' (*sensu* Brown and Solar, 1999; Brown *et al.*, 2011) of the middle Carboniferous magmatic arc. The emplacement depth is consistent with crustal recycling during formation of upper Palaeozoic granites in northern Chile (Lucassen *et al*., 1999), and the geothermal gradient of 52 °C/km deduced from the metamorphic P-T conditions is coherent with upper crust (<10 km) geothermal gradients in continental magmatic arcs (*e.g*., Rothstein and Manning, 2003) and with gradients associated with the formation of low-pressure/high-temperature metamorphic belts (De Yoreo *et al.*, 1991; Takeshita and Okudaira, 1995).

The 'Toco Orogeny' (Bahlburg and Breitkreuz, 1991) affected all Upper Devonian-Lower Carboniferous metasedimentary units in the Coastal Cordillera of northern Chile, which were folded, deformed, and slightly metamorphosed (Bahlburg and Hervé, 1997). These authors suggested that this deformation proceeded as the units were incorporated into the Carboniferous accretionary prism of SW Gondwana. While the maximum age of this deformative event is constrained by the youngest U-Pb detrital zircon age population in these metasedimentary successions (*ca.* 350 Ma: El Toco Formation, Augustsson *et al*., 2015; *ca*. 335 Ma: Sierra del Tigre Formation, Antofagasta Minerals *in* Baeza and Astudillo, 2019), the minimum age is restricted by undeformed Upper Carboniferous granites that intrude the El Toco Formation. These plutonic bodies were dated using K-Ar in biotite at *ca.* 320-310 Ma (Maksaev and Marinovic, 1980; Skarmeta and Marinovic, 1981; Lucassen *et al.*, 1999). However, more precise U-Pb zircon dating in recent years has yielded ages of *ca.* 302-301 Ma

(Sepúlveda *et al.*, 2014; Vásquez *et al.*, 2018), indicating a pre-Late Pennsylvanian (Gzhelian) age for the Toco tectonic event.

Considering the Early-Middle Mississippian maximum age for the 'Toco Orogeny', the formation of migmatites of the CLMC at *ca.* 318-316 Ma (Early Pennsylvanian), and the emplacement of undeformed plutonic bodies at *ca.* 302-301 Ma (Late Pennsylvanian), it is highly probable that the compressional deformative event recorded in the CLMC was essentially coeval with the 'Toco Orogeny'. Moreover, as shown here, the abundant kinematic indicators of syn-anatectic strain in the CLMC (Fig. 2; Appendix B) show an approximately westward (current coordinates) tectonic transport, which is nearly the same vergence of folds and faults affecting the El Toco and Sierra del Tigre formations. The latter units exhibit gently plunging overturned to recumbent chevron folds and minor concentric folds, with axial planes with NW to NNW trends and 0° to 30° NE dips, and sub-horizontal SW-vergent thrust faults (Maksaev and Marinovic, 1980; Boric, 1981; Skarmeta and Marinovic, 1981; Niemeyer *et al.*, 1997), which, in sum, indicate an overall WSW- to SW-vergence. These chronological and structural similarities, together with the fact that no other Carboniferous tectonic events have so far been reported from this segment of the SW Gondwana margin, allow us to infer that the tectonic event recorded during the generation of the migmatites of the CLMC was, in fact, the 'Toco Orogeny'. This would constrain the age of this tectonic event to the Early Pennsylvanian.

Taking into account the Early Mississippian (*ca.* 350 Ma) maximum depositional age of the El Toco Formation, and the Early Pennsylvanian (*ca.* 318-316 Ma) migmatisation age of the CLMC, forearc tectonic and sedimentary processes could have acted over up to ~30 Myr, which saw incorporation of the sediments of the El Toco Formation into the upper crust and development of migmatites at ~13 km. The forearc thermal anomaly responsible for the generation of the CLMC is evidently associated with a compressional tectonic regime, as shown by the kinematic indicators, a regime that contrasts with the extensional scenarios proposed by Creixell *et al.* (2021). Niemeyer *et al.* (1997) also found evidence of extensional tectonic deformation in rocks of the Sierra del Tigre Formation but showed that it developed in soft sediments and was later overprinted by the SW-vergent compressive tectonic deformation, which they attributed to its subsequent incorporation into the accretionary prism. A minimum thickness of ~2,300 m has been determined for the El Toco and Sierra del Tigre formations (Bahlburg and Breitkreuz, 1993; Niemeyer *et al.*, 1997). The depth of ~13 km for the migmatisation event necessarily implies a relatively fast increase in the crustal thickness of the forearc, which would require tectonics prevailing over sedimentary processes, with the former likely to be linked to thrusting of these units during the geodynamic evolution of the forearc. This is consistent with the inferred compressive tectonics during the migmatisation of the CLMC. The thermal input required to modify the geothermal gradient in the forearc and allow migmatisation in the upper crust must derive from the advection of heat of contemporaneous magmas (*e.g.*, Brown, 2013), most likely from the mantle or lower crust of SW Gondwana. There is currently no evidence to support other extra-continental sources of heat, such as subduction of a young oceanic plate or a spreading ridge.

Another case of Pennsylvanian migmatite formation at the SW Gondwana margin was recorded farther south (~33°S), at Las Cruces on the coast of central Chile, where Hervé *et al.* (2020) dated a garnet-bearing granitic neosome at *ca.* 320 Ma (U-Pb SHRIMP zircon age) and inferred a forearc tectonic setting for its sedimentary protolith. Despite the sparse evidence of such high-T metamorphic processes, it seems that migmatite formation in the forearc of the SW Gondwana margin was linked to major changes in subduction system dynamics, in connection with either the start of subduction in the Early Carboniferous (*ca.* 340-330 Ma; Creixell *et al.*, 2021) or the end of the Devonian magmatic lull (Bahlburg, 2022).

6. Conclusions

Migmatites of the CLMC formed at ~3.3-3.4 kbar and 650 °C. Kinematic indicators suggest compressional tectonic conditions during their generation in the Early Pennsylvanian (318-316 Ma). The inferred depth of the CLMC migmatisation event (~13 km) is coherent with that determined for coeval intrusive rocks cropping out in the Precordillera. It markedly contrasts with the shallower depths of post-Middle Pennsylvanian intrusive bodies emplaced in the upper crust of SW Gondwana.

U-Pb detrital zircon ages indicate that both the El Toco Formation and the protolith of the CLMC have maximum depositional ages in the Early Mississippian (*ca*. 350 Ma). The similarities in their overall U-Pb detrital zircon age pattern, and the proximity of their outcrops, suggest that the protolith of the CLMC is the El Toco Formation. These rocks were deposited at the margin of SW Gondwana and subsequently incorporated into the upper crust of the forearc by tectonic processes during the early-middle Carboniferous. Later anatexis of this unit occurred in the Early Pennsylvanian, associated with compressional tectonic conditions.

The structural similarities between the deformation registered in the CLMC and those present in the El Toco and Sierra del Tigre formations, together with their temporal constraints, allow us to infer that the 'Toco Orogeny' was the cause of the compressional tectonic conditions recorded during the generation of the migmatites of the CLMC in the Early Pennsylvanian.

The metamorphic P-T conditions determined for the CLMC imply that the structure that currently separates this unit from the El Toco Formation (the AFS) represents a major structural discontinuity. Prior to the Late Triassic, the CLMC was uplifted along this fault relative to the El Toco Formation outcrops, resulting in the juxtaposition of rocks with contrasting metamorphic conditions.

Acknowledgments

This study is part of the Chilean National Mapping Program (PNG) of the General Geology Department at Sernageomin. We are very grateful for the inspiration and support that "Pancho" Hervé gave us during all these years. We are indebted to F. Lucassen for access to his samples of the CLMC. M. Calderón (Universidad del Desarrollo), H.-J. Massonne (Stuttgart Universität), and J. Álvarez (Sernageomin) are thanked for helping in thermodynamic calculations. C. Holmgren and E. Fonseca (Sernageomin) for assistance with opaque minerals petrography. A. Tomlinson (Sernageomin) for field support and fruitful discussions. F. LIona and A. Bustos (Sernageomin) performed the LA-ICP-MS analysis. M. Suárez (Sernageomin) conducted the EDS analyses. Thorough reviews by H. Bahlburg, C. Casquet, A. Willner, and editorial handling by R.J. Pankhurst and D. Bertin helped to greatly improve the original text.

References

Aguilef, S.; Franco, C.; Tomlinson, A.J.; Blanco, N.; Álvarez, J.; Montecino, D.; Gardeweg, M.; Campos, V.; Rodríguez, C.; Maksaev, V.; Bobadilla, H.; Vásquez, P.; Grunder, A.L.; Dilles, J.H. 2019. Geología del área Quehuita-Chela, regiones de Tarapacá y Antofagasta. Servicio Nacional de Geología y Minería, Carta Geológica de Chile, Serie Geología Básica 207: 293 p., 1 mapa escala 1:100.000. Santiago.

Augustsson, C.; Rüsing, T.; Niemeyer, H.; Kooijman, E.; Berndt, J.; Bahlburg, H.; Zimmermann, U. 2015. 0.3 byr of drainage stability along the Palaeozoic palaeo-Pacific Gondwana margin; a detrital zircon study. Journal of the Geological Society 172 (2): 186-200. https://doi.org/10.1144/jgs2014-065

Baeza, L.; Astudillo, N. 2019. Carta Pedro de Valdivia, región de Antofagasta. Servicio Nacional de Geología y Minería, Carta Geológica de Chile, Serie Geología Básica 206: 91 p., 1 mapa escala 1:100.000. Santiago.

Bahlburg, H. 1987a. Geochemical Features of Devonian/ Carboniferous Flysch Greywackes of the North Chilean Coastal Cordillera. Zentralblatt für Geologie und Paläontologie, Teil 1 (7/8): 893-904. Stuttgart.

Bahlburg, H. 1987b. Sedimentology, petrology and geotectonic significance ofthe Paleozoic flysch in the Coastal Cordillera of northern Chile. Neues Jahrbuch für Geologie und Paläontologie - Monatshefte 1987 (9): 527-559.

Bahlburg, H. 2022. A Silurian-Devonian active margin in the proto-Andes - new data on an old conundrum. International Geology Review 64 (21): 3099-3120. https://doi.org/10.1080/00206814.2021.2012719

Bahlburg, H.; Breitkreuz, C. 1991. The evolution of marginal basins in the southern Central Andes of Argentina and Chile during the Paleozoic. Journal of South American Earth Sciences 4: 171-188.

Bahlburg, H.; Breitkreuz, C. 1993. Differential response of a Devonian-Carboniferous platform-deeper basin system to sea-level change and tectonics, N. Chilean Andes. Basin Research 5 (1): 21-40. https://doi.org/10.1111/j.1365-2117.1993.tb00054.x

Bahlburg, H.; Hervé, F. 1997. Geodynamic evolution and tectonostratigraphic terranes of northwestern Argentina and northern Chile. Geological Society of America, Bulletin 109 (7): 869-884. https://doi.org/10.1130/0016-7606(1997)109%3C0869:GEATTO%3E2.3.CO;2

Bahlburg, H.; Vervoort, J.; Du Frane, S.; Bock, B.; Augustsson, C.; Reimann, C. 2009. Timing of crust formation and recycling in accretionary orogens:

Insights learned from the western margin of South America. Earth-Science Reviews 97 (1-4): 215-241. https://doi.org/10.1016/j.earscirev.2009.10.006

Black, L.P.; Kamo, S.L.; Allen, C.M.; Davis, D.W.; Aleinikoff, J.N.; Valley, J.W.; Mundil, R.; Campbell, I.H.; Korsch, R.J.; Williams, I.S.; Foudoulis, C. 2004. Improved $^{206}Pb/^{218}U$ microprobe geochronology by the monitoring of a trace-element-related matrix effect; SHRIMP, ID-TIMS, ELA-ICP-MS and oxygen isotope documentation for a series of zircon standards. Chemical Geology 205 (1-2): 115-140. https://doi.org/10.1016/j.chemgeo.2004.01.003

Bobenrieth, L. 1980. Geología de los cuadrángulos Cerro Desamparado y Cerro Soledad, Regiones de Tarapacá y Antofagasta. Tesis de grado, Universidad de Chile, Departamento de Geología: 171 p. Santiago.

Boedo, F.; Willner, A.P.; Vurjovich, G.I.; Massonne, H-.J. 2016. High-pressure/low-temperature metamorphism in the collision zone between the Chilenia and Cuyania microcontinents (western Precordillera, Argentina). Journal of South American Earth Sciences 72: 227-240. https://doi.org/10.1016/j.jsames.2016.09.009

Boric, R. 1981. Geología de los cuadrángulos Estación Colupito y Toco, región de Antofagasta. Instituto de Investigaciones Geológicas, Carta Geológica de Chile 49-50: 52 p., 2 mapas escala 1:50.000. Santiago.

Breitkreuz, C.; Bahlburg, H. 1985. Palaeozoic Flysch Series in the Coastal Cordillera of Northern Chile. Geologische Rundschau 74 (3): 565-572. https://doi.org/10.1007/bf01821212

Brown, M. 2013. Granite: From genesis to emplacement. Geological Society of America, Bulletin 125 (7-8): 1079-1113. https://doi.org/10.1130/B30877.1

Brown, M.; Solar, G.S. 1999. The mechanism of ascent and emplacement of granite magma during transpression: a syntectonic granite paradigm. Tectonophysics 312 (1): 1-33. https://doi.org/10.1016/S0040-1951(99)00169-9

Brown, M.; Korhonen, F.J.; Siddoway, C.S. 2011. Organizing melt flow through the crust. Episodes 7 (4): 261-266. https://doi.org/10.2113/gselements.7.4.261

Calderón, M.; Hervé, F.; Munizaga, F.; Pankhurst, R.J.; Fanning, C.M.; Rapela, C.W. 2020. Geochronological record of plutonic activity on a long-lived active continental margin, with emphasis on the pre-Andean rocks of Chile. *In* Geocronologia e Evolução Tectônica do Continente Sul-Americano: a contribuição de Umberto Giuseppe Cordani (Bartorelli, A.; Teixeira, W.; De Brito Neves, B.B.; editors.). Solaris Edições Culturais, Capítulo18: 392-407. São Paulo.

Calle, A.Z.; Horton, B.K.; García, R.; Anderson, R.B.; Stockli, D.F.; Flaig, P.P.; Long, S.P. 2023. Sediment Dispersal and Basin Evolution During Contrasting Tectonic Regimes Along the Western Gondwanan Margin in the Central Andes. Journal of South American Earth Sciences 125: 104286. https://doi.org/10.1016/j.jsames.2023.104286

Cardona, A.; Cordani, U.G.; Ruiz, J.; Valencia, V.A.; Armstrong, R.; Chew, D.; Nutman, A.; Sánchez, A.W. 2009. U-Pb zircon geochronology and Nd isotopic signatures of the pre-Mesozoic metamorphic basement of the eastern Peruvian Andes: growth and provenance of a late Neoproterozoic to carboniferous accretionary orogen on the northwest margin of Gondwana. Journal of Geology 117 (3): 285-305. https://doi.org/10.1086/597472

Cawood, P.A. 2005. Terra australis Orogen: Rodinia breakup and development of the Pacific and Iapetus margins of Gondwana during the Neoproterozoic and Paleozoic. Earth Science Reviews 69 (3-4): 249-279. https://doi.org/10.1016/j.earscirev.2004.09.001

Charrier, R.; Pinto, L.; Rodríguez, M.P. 2007. Tectonostratigraphic evolution of the Andean Orogen in Chile. *In* The Geology of Chile (Moreno, T.; Gibbons, W.; editors.). The Geological Society: 21-114. London.

Chen, D. 2010. Devonian-Carboniferous Carbonates around Guilin, South China: Stratigraphy and Sedimentology. *In* IGCP-580 Meeting, Applications of Magnetic Susceptibility on Paleozoic Rocks. Guidebook for field excursion: 29 p. Guilin.

Chen, D.; Qing, H. 2024. Devonian-Carboniferous Carbonates in Guilin, South China: Depositional Records of Platform-Basin Complex and Major Biocrisises. *In* Field Trip Guidebook on Chinese Sedimentary Geology (Hu, X.; editor). Springer: 809-871. Singapore.

Chew, D.M.; Schaltegger, U.; Košler, J.; Whitehouse, M.J.; Gutjahr, M.; Spikings, R.A.; Mišković, A. 2007. U-Pb geochronologic evidence for the evolution of the Gondwanan margin of the north-central Andes. Geological Society of America, Bulletin 119 (5-6): 697-711. https://doi.org/10.1130/B26080.1

Connolly, J.A.D. 2005. Computation of phase equilibria by linear programming: a tool for geodynamic modeling and its application to subduction zone decarbonation. Earth and Planetary Science Letters 236 (1-2): 524-541. https://doi.org/10.1016/j.epsl.2005.04.033

Creixell, C.; Sepúlveda, F.; Álvarez, J.; Vásquez, P.; Velásquez, R. 2021. The Carboniferous onset of subduction at SW Gondwana revisited: Sedimentation and deformation processes along the late Paleozoic

forearc of north Chile (21°-33° S). Journal of South American Earth Sciences 107: 103149. https://doi.org/10.1016/j.jsames.2020.103149

Creixell, C.; Díaz-Alvarado, J.; Álvarez, J.; Rodríguez, C.; Velásquez, R.; Oliveros, V. 2025. Episodic magmatism and segmentation of the Gondwanan arc in Chile (21-38°S): Insights into Carboniferous to early Permian subduction processes and deformation. Journal of South American Earth Sciences 156: 105421. https://doi.org/10.1016/j.jsames.2025.105421

Dahlquist, J.A.; Alasino, P.H.; Basei, M.; Morales Cámera, M.; Macchioli Grande, M.; da Costa Campos Neto, M. 2018. Petrological, geochemical, isotopic, and geochronological constraints for the Late Devonian-Early Carboniferous magmatism in SW Gondwana (27-32° LS): an example of geodynamic switching. International Journal of Earth Sciences 107: 2575-2603.

Dahlquist, J.A.; Morales Cámera, M.M.; Alasino, P.H.; Pankhurst, R.J.; Basei, M.A.S.; Rapela, C.W.; Moreno, J.A.; Baldo, E.G.; Galindo, C. 2021. A review of Devonian-Carboniferous magmatism in the central region of Argentina, Pre-Andean margin of SW Gondwana. Earth-Science Reviews 221: 103781. https://doi.org/10.1016/j.earscirev.2021.103781

Dahlström, S.I.R.; Cooper, F.J.; Blundy, J.; Tapster, S.; Yáñez, J.C.; Evenstar, L.A. 2022. Pluton exhumation in the Precordillera of northern Chile (17.8°-24.2° S): Implications for the formation, enrichment, and preservation of porphyry copper deposits. Economic Geology 117 (5): 1043-1071. https://doi.org/10.5382/econgeo.4912

Dalziel, I.W.D.; Forsythe, R.D. 1985. Andean evolution and the terrane concept. *In* Tectonostratigraphic terranes of the Circum-Pacific-Region (Howell, D.G.; editor). Circum-Pacific-Council for Energy and Mineral Resources, Earth Science Series 1: 565-581.

Damm, K.W.; Pichowiak, S.; Harmon, R.S.; Todt, W.; Kelley, S.; Omarini, R.; Niemeyer, H. 1990. Pre-Mesozoic evolution of the central Andes; The basement revisited. *In* Plutonism from Antarctica to Alaska (Kay, S.M.; Rapela, C.W.; editors.). Geological Society of America: 101-125. Boulder. https://doi.org/10.1130/SPE241-p101

De Yoreo, J.J.; Lux, D.R.; Guidotti, C.V. 1991. Thermal modelling in low-pressure/high-temperature metamorphic belts. Tectonophysics 188 (3-4): 209-238. https://doi.org/10.1016/0040-1951(91)90457-4

Díaz-Alvarado, J.; Galaz, G.; Oliveros, V.; Creixell, C.; Calderón, M. 2019. Fragments of the late Paleozoic accretionary complex in central and northern Chile: similarities and differences as a key to decipher the complexity of the late Paleozoic to Triassic early Andean events. *In* Andean Tectonics (Horton, B.; Folguera, A.; editors). Elsevier: 509-530.

Diener, J.F.A.; Powell, R. 2010. Influence of ferric iron on the stability of mineral assemblages. Journal of Metamorphic Geology 28 (6): 599-613. https://doi.org/10.1111/j.1525-1314.2010.00880.x

Einhorn, J.C.; Gehrels, G.E.; Vernon, A.; DeCelles, P.G. 2015. U-Pb zircon geochronology of Neoproterozoic-Paleozoic sandstones and Paleozoic plutonic rocks in the Central Andes (21°S-26° S). *In* Geodynamics of a Cordilleran Orogenic System: The Central Andes of Argentina and Northern Chile (DeCelles, P.G.; Ducea, M.N.; Carrapa, B.; Kapp, P.A.; editors). Geological Society of America, Memoir 212: 115-124. https://doi.org/10.1130/2015.1212(06)

Ferraris, F.; Di Biase, F. 1978. Hoja Antofagasta, región de Antofagasta. Instituto de Investigaciones Geológicas, Carta Geológica de Chile 30: 48 p., 1 mapa escala 1:250.000. Santiago.

Ferroni, F.; DeCelles, P.G.; Veramendi, J.O.; Dahlquist, J.A.; di Pasquo, M. 2025. New Geochronological Constraints on the Late Palaeozoic Tarija Basin, Southern Bolivia: Tectonic and Palaeoclimatic Implications. Terra Nova 38 (1): 9-18. https://doi.org/10.1111/ter.70007

García Zavaleta, A.; Hauser, N.; Roddaz, M.; Gonçalves, G.O.; Aparicio González, P.; Baby, P.; Reimold, W.U.; Puma, F.; Bravo, P.; Humerez, M. 2024. Provenance of Devonian-Carboniferous Sedimentary Rocks of the Tarija Basin, Southern Bolivia: Implications for the Geodynamic Evolution of the Southwestern Margin of Gondwana. Geological Society of America, Bulletin 136 (3-4): 1730-1752. https://doi.org/10.1130/B36701.1

Grocott, J.; Taylor, G.K. 2002. Magmatic arc fault systems, deformation partitioning, and the emplacement of granitic complexes in the Coastal Cordillera, north Chilean Andes (25-27° S). Journal of Geological Society of London 159 (4): 425-442. https://doi.org/10.1144/0016-764901-124

Harrington, H.J. 1961. Geology of parts of Antofagasta and Atacama provinces of northern Chile. American Association of Petroleum Geologist, Bulletin 45 (2): 168-197. https://doi.org/10.1306/0BDA6332-16BD-11D7-8645000102C1865D

Hawthorne, F.C.; Oberti, R.; Harlow, G.E.; Maresch, W.V.; Martin, R.F.; Schumacher, J.C.; Welch, M.D. 2012. IMA report: nomenclature of the amphibole supergroup. American Mineralogist 97 (11-12): 2031-2048. https://doi.org/10.2138/am.2012.4276

Hemmelmann, A. 2018. Petrologie und Mineralchemie des metamorphen andinen Basements bei Caleta Loa, Nordchile. Bachelorarbeit (Unveröffentlichte), Technische Univeristät Berlin: 56 p.

Henry, D.J.; Guidotti, C.V.; Thomson, J.A. 2005. The Ti-saturation surface for low-to-medium pressure metapelitic biotites: implications for geothermometry and Ti-substitution mechanisms. American Mineralogist 90 (2-3): 316-328. https://doi.org/10.2138/am.2005.1498

Hervé, F.; Faúndez, V.; Calderón, M.; Massonne, H.-J.; Willner, A.P.; Moreno, T. 2007. Metamorphic and plutonic basement complexes. *In* The Geology of Chile (Gibbons, W.; editor). The Geological Society: 5-20. London.

Hervé, F.; Calderón, M.; Fanning, C.M.; Pankhurst, R.J.; Godoy, E. 2013. Provenance variations in the Late Paleozoic accretionary complex of central Chile as indicated by detrital zircons. Gondwana Research 23: 1122-1135.

Hervé, F.; Calderón, M.; Fanning, C.M.; Pankhurst, R.J.; Navarro, J. 2020. U-Pb SHRIMP detrital zircon dating of metamorphic rocks in north-central Chile (28°-33° S): evidence for Carboniferous and Triassic metamorphism in a subduction setting. Journal of South American Earth Science 103: 102767. https://doi.org/10.1016/j.jsames.2020.102767

Holland, T.J.B.; Powell, R. 1991. A Compensated-Redlich-Kwong (CORK) equation for volumes and fugacities of CO_2 and H_2O in the range 1 bar to 50 kbar and 100-1600 °C. Contributions to Mineralogy and Petrology 109: 265-273.

Holland, T.J.B.; Powell, R. 1998. An internally consistent thermodynamic data set for phases of petrological interest. Journal of Metamorphic Geology 16 (3): 309-343. https://doi.org/10.1111/j.1525-1314.1998.00140.x

Holness, M.; Cesare, B.; Sawyer, E.W. 2011. Melted rocks under the microscope: microstructures and their interpretation. Elements 7 (4): 247-252. https://doi.org/10.2113/gselements.7.4.247

Jackson, S.E.; Pearson, N.J.; Griffin, W.L.; Belousova, E.A. 2004. The application of laser ablation-inductively coupled plasma-mass spectrometry to *in situ* U-Pb zircon geochronology. Chemical Geology 211 (1-2): 47-69. https://doi.org/10.1016/j.chemgeo.2004.06.017

Loewy, S.; Connelly, J.; Dalziel, I. 2004. An orphaned basement block: The Arequipa-Antofalla Basement of the central Andean margin of South America. Geological Society of America, Bulletin 116 (1-2): 171-187. https://doi.org/10.1130/B25226.1

Lucassen, F.; Laber, A.; Franz, G. 1994. Geology and petrology of metamorphic rocks from the Preandean basement of northern Chile, 18°-24° S. *In* Congreso Geológico Chileno, No. 7, Actas I: 96-100. Concepción.

Lucassen, F.; Wilke, H.-G.; Virarnonte, J.; Becchio, R.; Franz, G.; Laber, A.; Wernmer, K.; Vroon, P. 1996. The paleozoic basement of the central andes (18°-26° S): a metamorphic view. *In* International Symposium on Andean Geodynamics, No. 3, Abstract: 779-782. St. Malo.

Lucassen, F.; Franz, G.; Thirlwall, M.F.; Mezger, K. 1999. Crustal recycling of metamorphic basement: late Palaeozoic granitoids of northern Chile (~22◦ S). Implications for the composition of the Andean crust. Journal of Petrology 40 (10): 1527-1551.

Lucassen, F.; Becchio, R.; Wilke, H.G.; Franz, G.; Thirlwall, M.F.; Viramonte, J.; Wemmer, K. 2000. Proterozoic-Paleozoic development of the basement of the Central Andes (18-26° S) - a mobile belt of the South American craton. Journal of South American Earth Sciences 13 (8): 697-715. https://doi.org/10.1016/S0895-9811(00)00057-2

Lucassen, F.; Becchio, R.; Harmon, R.; Kasemann, S.; Franz, G.; Trumbull, R.; Wilke, H.G.; Romer, R.L.; Dulski, P. 2001. Composition and density model of the continental crust at an active continental margin: The Central Andes between 21° and 27° S. Tectonophysics 341 (1-4): 195-223. https://doi.org/10.1016/S0040-1951(01)00188-3

Ludwig, K.R. 2012. User`s manual for Isoplot, Version 3.75, A geochronological toolkit for Microsoft Excel. Berkeley Geochronology Center, Special Publication 5: 75 p. California.

Maksaev, V.; Marinovic, N. 1980. Geología de los Cuadrángulos Cerro de la Mica, Quillagua, Cerro Posada y Oficina Prosperidad, región de Antofagasta. Instituto de Investigaciones Geológicas, Carta Geológica de Chile 45-48: 63 p., 4 mapas escala 1:50.000. Santiago.

Maksaev, V.; Munizaga, F.; Tassinari, C. 2014. Timing of the magmatism of the paleo-Pacific border of Gondwana: U-Pb geochronology of Late Paleozoic to Early Mesozoic igneous rocks of the north Chilean Andes between 20° and 31° S. Andean Geology 41 (3): 447-506. http://dx.doi.org/10.5027/andgeoV41n3-a01

Massonne, H.-J. 2013. Constructing the pressure-temperature path of ultrahigh-pressure rocks. Elements 9 (4): 267-279. https://doi.org/10.2113/gselements.9.4.267

Massonne, H.-J.; Willner, A.P.; Gerya, T. 2007. Densities of metapelitic rocks at high to ultrahigh pressure

conditions: what are the geodynamic consequences? Earth and Planetary Science Letters 256 (1-2): 12-27. https://doi.org/10.1016/j.epsl.2007.01.013

Moisan, P.; Niemeyer, H.; Kerp, H. 2011. Lycopsids from the Upper Devonian of northern Chile with remarks on the geographical distribution of the morphogenus *Haplostigma* Seward. Paläontologische Zeitschrift 85: 231-240.

Mpodozis, C.; Ramos, V.A. 1989. The Andes of Chile and Argentina. *In* Geology of the Andes and its relation to hydrocarbon and mineral resources (Ericksen, G.E.; Cañas Pinochet, M.T.; Reinemund, J.A.; editors). Circum Pacific Council for Energy and Mineral Resources, Earth Science Series 11: 59-90.

Niemeyer, H.; Venegas, R.; González, C.; Aceñolaza, F. 1997. Los terrenos paleozoicos del Salar de Navidad, Región de Antofagasta, Chile. Revista Geológica de Chile 24 (2): 123-143.

Pankhurst, R.J.; Rapela, C.W.; Saavedra, J.; Baldo, E.; Dahlquist, J.; Pascua, I.; Fanning, C.M. 1998. The Famatinian magmatic arc in the southern Sierras Pampeanas: an Early to Mid-Ordovician continental arc on the Gondwana margin. *In* The Proto-Andean Margin of Gondwana (Pankhurst, R.J.; Rapela, C.W.; editors). Special Publication of the Geological Society, London 142: 343-367. https://doi.org/10.1144/GSL.SP.1998.142.01.17

Pankhurst, R.; Hervé, F.; Fanning, C.M.; Calderón, M.; Niemeyer, H.; Griem-Klee, S.; Soto, F. 2016. The pre-Mesozoic rocks of northern Chile: U-Pb ages, and Hf and O isotopes. Earth-Science Reviews 152: 88-105. https://doi.org/10.1016/j.earscirev.2015.11.009

Pawley, M.; Reid, A.; Dutch, R.; Preiss, W. 2015. Demystifying migmatites: introduction for field-based geologist. Applied Earth Science 124 (3): 147-174. https://doi.org/10.1179/1743275815Y.0000000014

Petrus, J.A.; Kamber, B.S. 2012. VizualAge: A novel approach to laser ablation ICP-MS U-Pb geochronology data reduction. Geostandards and Geoanalytical Research 36 (3): 247-270. https://doi.org/10.1111/j.1751-908X.2012.00158.x

Powell, R.; Holland, T. 1999. Relating formulations of the thermodynamics of mineral solid solutions: activity modeling of pyroxenes, amphiboles and micas. American Mineralogist 84: 1-14.

Ramos, V.A. 2008. The Basement of the Central Andes: The Arequipa and Related Terranes. Annual Review of Earth and Planetary Sciences 36: 289-324. https://doi.org/10.1146/annurev.earth.36.031207.124304

Ramos, V.A. 2009. Anatomy and global context of the Andes: Main geologic features and the Andean orogenic cycle. *In* Backbone of the Americas: Shallow Subduction, Plateau Uplift, and Ridge and Terrane Collision (Kay, S.M.; Ramos, V.A.; Dickinson, W.R., editors). Geological Society of America Memoir 204: 31-65. https://doi.org/10.1130/2009.1204(02)

Ramos, V.A. 2010. The Grenville-age basement of the Andes. Journal of South American Earth Sciences 29 (1): 77-91. https://doi.org/10.1016/j.jsames.2009.09.004

Ramos, V.A.; Jordan, T.E.; Allmendinger, R.W.; Mpodozis, C.; Kay, S.; Cortés, J.M.; Palma, M. 1986. Paleozoic terranes of the central Argentine-Chilean Andes. Tectonics 5 (6): 855-880. https://doi.org/10.1029/TC005i006p00855

Rapela, C.W.; Pankhurst, R.J.; Casquet, C.; Dahlquist, J.A.; Fanning, C.M.; Baldo, E.G.; Galindo, C.; Alasino, P.H.; Ramacciotti, C.D.; Verdecchia, S.O.; Murra, J.A.; Basei, M.A.S. 2018. A review of the Famatinian Ordovician magmatism in southern South America: evidence of lithosphere reworking and continental subduction in the early proto-Andean margin of Gondwana. Earth-Science Reviews 187: 259-285. https://doi.org/10.1016/j.earscirev.2018.10.006

Reimann, C.R.; Bahlburg, H.; Kooijman, E.; Berndt, J.; Gerdes, A.; Carlotto, V.; López, S. 2010. Geodynamic evolution of the early Paleozoic Western Gondwana margin 14-17° S reflected by the detritus of the Devonian and Ordovician basins of southern Peru and northern Bolivia. Gondwana Research 18 (2-3): 370-384. https://doi.org/10.1016/j.gr.2010.02.002

Rothstein, D.A.; Manning, C.E. 2003. Geothermal gradients in continental magmatic arcs: constraints from the eastern Peninsular Ranges Batholith, Baja California, Mexico. Geological Society of America, Special Paper 374: 337-354. https://doi.org/10.1130/0-8137-2374-4.337

Sawyer, E.W. 2008. Atlas of Migmatites. The Canadian Mineralogist, Special Publication 9. NRC Research Press, Ottawa, Ontario, Canada. https://doi.org/10.1139/9780660197876

Scheuber, E.; González, G. 1999. Tectonics of the Jurassic Early Cretaceous magmatic arc of the north Chilean Coastal Cordillera (22°-26°S): A story of crustal deformation along a convergent plate boundary. Tectonics 18 (5): 895-910. https://doi.org/10.1029/1999TC900024

Sepúlveda, F.A.; Vásquez, P.; Quezada, A. 2014. Cartas Patillos y Oficina Victoria, región de Tarapacá. Servicio Nacional de Geología y Minería, Carta Geológica de Chile, Serie Geología Básica 167-168: 125 p., 1 mapa escala 1:100.000. Santiago.

Sepúlveda, F.; González, E.; Tomlinson, A.J. 2024. Geología y estructura del cuadrángulo Quebrada Arcas, región de Antofagasta, Chile. Servicio Nacional de Geología y Minería, Informe Registrado IR-23-108 (inédito): 53 p., 1 mapa escala 1:50.000. Santiago.

Sernageomin. 2002. Mapa Geológico de Chile. Carta Geológica de Chile, Serie Geología Básica 75, 1 mapa en 3 hojas, escala 1:1.000.000. Santiago.

Skarmeta, J.; Marinovic, N. 1981. Geología de la Hoja Quillagua, región de Antofagasta. Instituto de Investigaciones Geológicas, Carta Geológica de Chile 51: 63 p., 1 mapa escala 1:250.000. Santiago.

Stevens, G.; Villaros, A.; Moyen, J.-F. 2007. Selective peritectic garnet entrainment as the origin of geochemical diversity in S-type granites. Geology 35 (1): 9-12. https://doi.org/10.1130/G22959A.1

Suárez, M.; Ramírez, C.; Cortés, R.; Llona, F.; Creixell, C.; Ramírez, A.; Vásquez, C. 2015. Desarrollo de una nueva técnica de separación de circones mediante la incorporación de fluorescencia en estudios de datación U-Pb. *In* Congreso Geológico Chileno, No. 14, Actas I: 703-706. La Serena.

Takeshita, T.; Okudaira, T. 1995. Dynamics and thermal modeling in low-pressure/high-temperature metamorphic belts. Journal of the Seismological Society of Japan, Second Series 47 (4): 453-467.

Torsvik, T.H.; Cocks, L.R.M. 2013. Gondwana from top to base in space and time. Gondwana Research 24 (3-4): 999-1030. https://doi.org/10.1016/j.gr.2013.06.012

Vásquez, P.; Sepúlveda, F.; Quezada, A.; Franco, C.; Blanco, N. 2018. Cartas Guanillos del Norte y Salar de Llamara, regiones de Tarapacá y Antofagasta. Servicio Nacional de Geología y Minería, Carta Geológica de Chile, Serie Geología Básica 195-196: 93 p., 1 mapa escala 1:100.000. Santiago.

Vaughan, A.P.M.; Leat, P.T.; Pankhurst, R.J. 2005. Terrane processes at the margins of Gondwana: an introduction. Geological Society, Special Publication 246: 1-22. London. https://doi.org/10.1144/GSL.SP.2005.246

Vermeesch, P. 2018. IsoplotR: a free and open toolbox for geochronology. Geoscience Frontiers 9 (5): 1479-1493.

Vermeesch, P. 2021. Maximum depositional age estimation revisited. Geoscience Frontiers 12 (2): 843-850. https://doi.org/10.1016/j.gsf.2020.08.008

White, R.W.; Powell, R.; Holland, T.J.B. 2001. Calculation of partial melting equilibria in the system Na_2O-$CaOK_2O$-FeO-MgO-Al_2O3-SiO_2-H_2O (NCKFMASH). Journal of Metamorphic Geology 19 (2): 139-153. https://doi.org/10.1046/j.0263-4929.2000.00303.x

White, R.W.; Pomroy, N.E.; Powell, R. 2005. An *in situ* metatexite-diatexite transition in upper amphibolite facies rocks from Broken Hill, Australia. Journal of Metamorphic Geology 23 (7): 579-602. https://doi.org/10.1111/j.1525-1314.2005.00597.x

Wilke, H.; Lucassen, F.; Wemmer, H. 1997. Chemistry and isotopic ages of metamorphic basement and intrusions. *In* Congreso Geológico Chileno, No. 8, Actas 2: 1593-1597. Antofagasta.

Williams, I.S. 1998. U-Th-Pb geochronology by ion microprobe. *In* Applications of Microanalytical Techniques to Understanding Mineralizing Processes (McKibben, M.A.; Shanks III, W.C.; Ridley, W.I.; editors). Reviews in Economic Geology 7: 1-35. https://doi.org/10.5382/Rev.07.01

Wu, C.M.; Chen, H.X. 2015. Revised Ti-in-biotite geothermometer for ilmenite- or rutile-bearing crustal metapelites. Science Bulletin 60 (1): 116-121. https://doi.org/10.1007/s11434-014-0674-y

Manuscript received: September 30, 2025; revised/accepted: May 08, 2026; available online: May 12, 2026.

Appendix A: Whole rock and mineral chemistry methodologies

1. Whole-rock geochemistry

Geochemical analyses of sample GSS-31 were performed at Activation Laboratories (Actlabs), Ontario, Canada. Weathered surfaces were removed, and fresh fragments were handpicked, crushed and pulverised in a steel mill (mild steel) to a fine powder of about 105 µm. The sample was prepared and analysed in a batch system, where it was mixed with a flux of lithium metaborate and lithium tetraborate, and treated by fusion technique. The sample was run for major oxides on a combination simultaneous/sequential analysis by ICP-OES (Agilent 5900) and ICP-MS (Agilent 7900). The standards used were NIST-694, NCS DC71305 (GBW 07113), NIST-696, DNC-1a, BHVO-2, W-2b, and SY-5, as reported by the laboratory. Detection limit for major oxides is 0.01 wt%, except for MnO and TiO_2, which are 0.005 wt% and 0.001 wt%, respectively. Laboratory procedures are described at www.actlabs.com (Actlabs code 4 LithoResearch).

Geochemical analyses of bulk rock composition of sample GSS-208 were performed at the Chemical Laboratory Unit of Sernageomin. Rock sample was grounded and pulverised below 60 µm. The pulverised sample was then mixed in a 1:3 ratio with a mixture of metaborate and lithium tetraborate, where the final ratio of sample:mixture was 1:10. A portion of the final mixture was prepared for major element analysis by X-ray Fluorescence (XRF), where it was fused into a glass bead. The concentration of major elements represented as percentage by weight of oxides was measured using a Panalytical AXIOS.

2. Mineral chemistry

Initially, SEM-EDS analyses of samples GSS-31 and GSS-208 were performed at the Scanning Electronic Microscopy Laboratory of Sernageomin, with a Zeiss EVO MA-10 equipped with an OXFORD X-ACT Instruments EDS detector. Samples were prepared with a carbon coating of 80 nm thickness. The instrument was set to 15 keV and 1.7 nA. The size of the scanning frame was adjusted to the respective grain size, with an average of 2.7 µm. Results are available in Supplementary Table 1).

Mineral chemical analyses of five selected samples (GSS-31, GSS-208, 3/276, 3/278, and 3/347) were obtained using an electron microprobe JEOL JXA-8530F of the Central Institution Electron Microscopy (ZELMI) at the Technische Universität Berlin. After an overview measurement by means of EDX analysis (energy-dispersive X-ray spectroscopy), the chemical composition of feldspar, garnet, biotite, sillimanite, amphibole, white mica (muscovite), chlorite, and opaque mineral was determined by wavelength-dispersive analysis (WDS). All elements were measured for 20 seconds (peak) and 10 seconds (background) at a current of 20 nA and an accelerating voltage of 15 kV. For all analyses, backscatter electron beams (BSE images) were created. The entire WDS results are provided in Supplementary Table 2).

Appendix B: Photographs of CLMC outcrops and shear indicators.

Syn-tectonic sigma porphyroblast showing top-to-the-west sense of shear. Feldspar porphyroblast (white in centre) has been rotated, with asymmetric strain shadows of quartz.

Asymmetric overturned folds indicating westward tectonic transport. Note leucosome located at the hinge of folds.

Overturned folds (upper centre) indicating westward vergence. Leucosome at the hinges is affected by S2 foliation (white line). Deformation is associated with reverse shear bands (dashed black lines).

Overturned to recumbent centimetric folds associated with a low-angle reverse shear band (centre) showing top-to-the west transport.

Slightly discordant leucosome veins at the upper part of the Loa canyon, with pinch-and-swell structure and millimetric melanocratic selvedge.